Review

Progress on Two-Dimensional Transitional Metal Dichalcogenides Alloy Materials: Growth, Characterisation, and Optoelectronic Applications

Jia Yu [1], Shiru Wu [1], Xun Zhao [1], Zhipu Li [1], Xiaowei Yang [1], Qian Shen [1], Min Lu [1,*], Xiaoji Xie [1], Da Zhan [2,3] and Jiaxu Yan [2,3,*]

1 Key Laboratory of Flexible Electronics (KLOFE), Institute of Advanced Materials (IAM), Nanjing Tech University, Nanjing 211816, China
2 Changchun Institute of Optics, Fine Mechanics & Physics (CIOMP), Chinese Academy of Sciences, Changchun 130033, China
3 University of Chinese Academy of Sciences, Chinese Academy of Sciences, Beijing 100049, China
* Correspondence: iammlv@njtech.edu.cn (M.L.); yanjiaxu@ciomp.ac.cn (J.Y.)

Abstract: Two-dimensional (2D) transitional metal dichalcogenides (TMDs) have garnered remarkable attention in electronics, optoelectronics, and hydrogen precipitation catalysis due to their exceptional physicochemical properties. Their utilisation in optoelectronic devices is especially notable for overcoming graphene's zero-band gap limitation. Moreover, TMDs offer advantages such as direct band gap transitions, high carrier mobility, and efficient switching ratios. Achieving precise adjustments to the electronic properties and band gap of 2D semiconductor materials is crucial for enhancing their capabilities. Researchers have explored the creation of 2D alloy phases through heteroatom doping, a strategy employed to fine-tune the band structure of these materials. Current research on 2D alloy materials encompasses diverse aspects like synthesis methods, catalytic reactions, energy band modulation, high-voltage phase transitions, and potential applications in electronics and optoelectronics. This paper comprehensively analyses 2D TMD alloy materials, covering their growth, preparation, optoelectronic properties, and various applications including hydrogen evolution reaction catalysis, field-effect transistors, lithium-sulphur battery catalysts, and lasers. The growth process and characterisation techniques are introduced, followed by a summary of the optoelectronic properties of these materials.

Keywords: two-dimensional materials; transitional metal dichalcogenides; alloy phase

1. Introduction

The miniaturisation of silicon-based transistors is approaching its physical limits, posing challenges for integrated circuits in terms of fundamental physical principles and high-power consumption. To sustain Moore's law, two-dimensional (2D) materials represented by transition metal dichalcogenides (TMDs) are expected to improve their high-density storage capabilities to achieve ultra-fast transmission characteristics. Their utilisation in optoelectronic devices is especially notable for surpassing graphene's limitation of lacking a band gap. Moreover, TMDs offer advantages such as direct band gap transitions, high carrier mobility, and efficient switching ratios. The accurate tuning of electronic properties and band gaps in 2D semiconductor materials is vital for enhancing their overall performance.

Researchers have explored the creation of 2D alloy phases through heteroatom doping, a strategy employed to fine-tune the band structure of these materials (Figure 1). The precise tuning of energy bands achieved by alloying engineering has led to the emergence of some photoelectric properties of 2D TMDs alloy materials. These attributes either remain absent in the original TMD materials or exhibit an elevated degree of excellence [1–5]. Their vibrational modes and photoluminescence peaks are affected by the alloying engineering,

and this attribute provides a new direction for the application of 2D TMDs alloy materials in hydrogen evolution reaction (HER) [6–8], field-effect transistors (FET) [9,10], lithium-sulphur battery catalysis [11,12], and lasers [13,14]. As the exploration of alloyed 2D TMD materials advances, its role in substantiating prospective strides in multifunctional materials for ensuing generation technologies becomes a discernible projection.
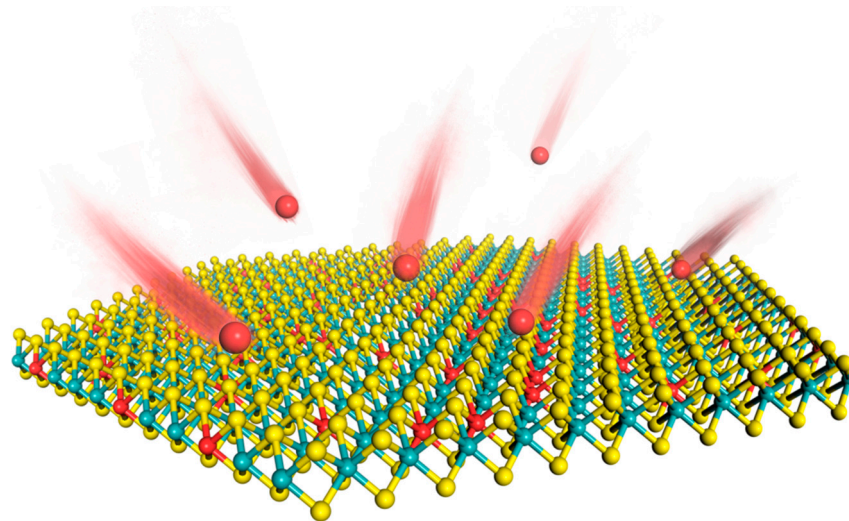

Figure 1. Creation of 2D alloy phases of TMD materials by doping with heteroatoms.

In this review, we first introduce the preparation and characterisation methods of 2D TMDs alloy materials. Then, we focus on their development and potential in various application areas. We look into the future of 2D TMDs alloy materials and point out the bottlenecks in their development.

2. Preparation and Characterisation of 2D TMDs Alloy Materials

The following sections present a methical outline of the techniques used for the preparation and characterisation of 2D alloy materials. The study begins by presenting various preparation processes, including mechanical stripping, chemical vapour deposition (CVD), physical vapour deposition (PVD), and chemical vapour transport (CVT). The advantages and disadvantages of each method are then compared and analysed. In addition, this article presents an introduction to the characterisation methods for 2D alloy materials. These methods include techniques for morphological analysis characterisation and spectral properties characterisation.

2.1. Preparation of 2D TMDs Alloy Materials

In laboratory settings, the preparation of 2D materials can be categorised into two primary methods: (1) Top-down, i.e., slowly tearing the lumpy layered TMDs material into a single- or few-layer material through mechanical peeling (dry method) and liquid phase etching substrate peeling (wet method). In the context of 2D semiconductor alloy materials, the typical approach involves synthesising the desired crystalline material through the CVT method. Subsequently, the material is subjected to shearing processes to yield single- or few-layer 2D materials. The disadvantage is that, in general, it is time-consuming and inefficient, and the final 2D layered material has a small area, which makes it not easy to control the uniform thickness of the sample, and the reproducibility is poor, making it difficult to operate in batch. (2) Bottom-up, including CVD and molecular methods. This method makes up for the shortcomings of the "top-down" approach and allows the preparation of large areas, high crystallinity, and a continuous atomic layer thickness of 2D TMDs. The CVD technique is presently the primary method employed in laboratories for producing 2D alloyed few-layer materials. This is due to its ability to yield high crystallinity, good homogeneity, and high controllability of samples [15]. Nevertheless,

the method's non-universal applicability is attributed to its limitations in meeting certain growth requirements.

2.1.1. Mechanical Stripping Method

The process of mechanical peeling involves the utilisation of an adhesive material, such as tape, to bind together crystalline materials. By applying mechanical force, the weak van der Waals forces between the layers of crystalline materials are disrupted, resulting in the thinning of the material. This results in the desired final single- or few-layer sample, as illustrated in Figure 2 [16,17].
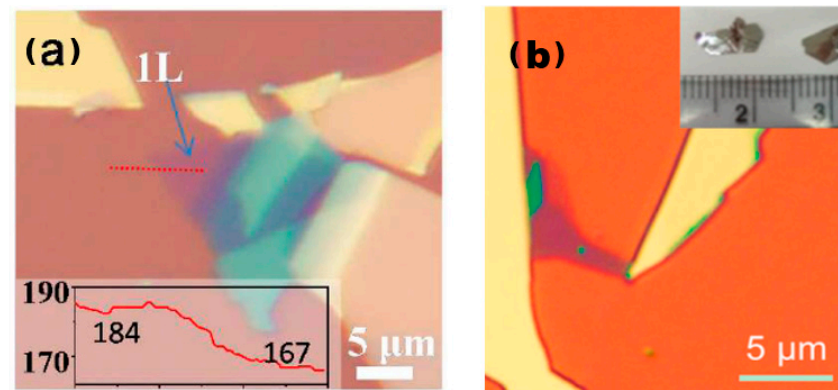

Figure 2. Atomic force microscopy images of 2D TMDs alloys prepared through mechanical exfoliation. (**a**) Optical image of exfoliated $Mo_{0.47}W_{0.53}S_2$ flakes on Si/SiO_2 substrate. Monolayer region is labelled as "1L". The inset shows red colour intensity along the red dashed line, giving a contrast of $(184-167)/184 = 9.2\%$ for the 1L. Reproduced with permission [16]. Copyright 2013, American Chemical Society; (**b**) optical image of $Mo_{0.67}W_{0.33}Se_2$ sheets. Inset in panel (**b**) is a photograph of $Mo_{0.67}W_{0.33}Se_2$ single crystals. Reproduced with permission [17]. Copyright 2014, American Chemical Society.

The mechanical peeling method is not significantly influenced by the material properties, and therefore, any block TMDs material that is prepared using the universal CVT method can be utilised to obtain the desired sample through this technique. Furthermore, since the prepared crystalline material is very crystalline and the peeling of the sample only destroys the van der Waals interactions between the layers, the surface of the final few-layer sample is not affected by problems such as improper handling during the preparation process, let alone the contamination of its surface by solvents, due to the fact that the whole process of mechanical peeling is a dry process. Therefore, mechanical peeling is often used in the study of the intrinsic properties of materials, making it one of the most important preparative tools in the study of the properties and applications of 2D materials.

However, in the process of sample preparation using the mechanical peeling method, the peeling by tape is very rough, and we can understand that the size, area, and thickness of the material cannot be perfectly adjusted precisely, especially in materials with strong interlayer van der Waals forces. It becomes more difficult to adjust the thickness by using this method. In addition, the size of the few-layer samples prepared through mechanical peeling is very small, which cannot fully satisfy the daily experimental conditions, and the thickness and size distribution of the samples on the substrate is also random, which is not conducive to large-scale application in electronic devices. In addition, the mechanical peeling of the sample and the substrate also becomes part of the residual glue, which also produces a certain degree of contamination. Although it can be erased through thermal annealing in a vacuum, this operation inevitably causes damage to the sample. In summary, these undesirable factors limit the prospects of the mechanical peeling method for the preparation of few-layer samples.

2.1.2. Chemical Vapour Deposition

The CVD method is a widely used technique for producing thin film materials. This method involves the chemical reaction of one or more gas-phase molecules on the surface of a substrate, resulting in the formation of thin film materials. It is generally divided into three reaction processes, namely, the formation of gas-phase molecules, the transfer of gas-phase molecules to the deposition area, and a reaction to form the target thin film sample. Here, we discuss and study the preparation of alloy materials by using the CVD method using $Mo_{1-x}W_xS_2$ as an example. In their study, Wang et al. utilised the low-pressure chemical vapour deposition technique to synthesise high-quality thin film materials of $Mo_{1-x}W_xS_2$ [18]. Figure 3a shows the reaction schematic of the sample prepared by using the CVD method. They used three precursors and substrates placed in the reaction system in a certain order, with components, purity, and content as follows: WCl_6 (99.9%, ~5 mg), sulphur (99%, 1.0 g), MoO_3 (>99.5%), and substrate (slide S1214). They were placed in a quartz tube with a diameter of 2 inches in the order shown in Figure 3c. The experiment utilised high-purity argon gas as the carrier gas. Four distinct temperature zones were employed to regulate the temperature of various precursors. The argon flow rate was adjusted to control the pressure. The temperature profile plot in Figure 3b illustrates the temperature distribution. There were three main stages. The first was the first 10 min of the warming stage, where the four precursors were warmed up to the set value temperature, i.e., WCl_6 was 35 °C, sulphur was 130 °C, MoO_3 was 520 °C, and the substrate was 700 °C, corresponding to an argon flow rate of 2000 sccm. Then, the next 15 min was the growth stage of the target film sample; here, it should be noted that WCl_6 grew gradually. During the cooling phase of the CVD reaction, WCl_6 was rapidly cooled to 15 °C for the final 5 min. Subsequently, the remaining components were cooled to room temperature once the entire CVD reaction had concluded. The final samples were processed, and they were transferred using a standard methyl methacrylate (PMMA)-assisted transfer method by spin-coating with PMMA, effectively separating the samples on the glass substrate with aqueous NaOH solution, then salvaging the PMMA-coated $Mo_{1-x}W_xS_2$ film samples through other substrates, and dissolving the PMMA using acetone. The thin film sample material was acquired as the final target (as shown in Figure 3d). The multilayer sample is represented by the bright area, while the monolayer sample is indicated by black lines in the figure. The substrate is depicted by the light brown area.

It should be noted that in this project, although the growth temperature of WS_2 was reduced to very close to that of MoS_2 by using highly volatile WCl_6 as a precursor, we could not completely avoid the formation of MoS_2/WS_2 heterostructures. This highlights a challenge in producing superior alloy materials using the CVD technique. In the process of growing 2D materials, the challenge of identifying source materials that can volatilise at lower temperatures results in a significant proportion of materials that cannot be synthesised through the CVD technique. Liu et al. [19] proposed that the molten salt-assisted method can be utilised to obtain the majority of TMDs 2D materials. The process reduces the melting point of metal precursors and facilitates their reaction with oxides to produce metal-aluminium oxides that are volatile. This enhances the accessibility of metal precursors to the gas phase, which simplifies the reaction. While the CVD method shows promise for producing metal sulphides, the resulting samples are currently inferior to those produced by using the stripping method. On the other hand, compared with the CVT method, CVD is not universal and is slightly inadequate in studying the intrinsic properties of materials.
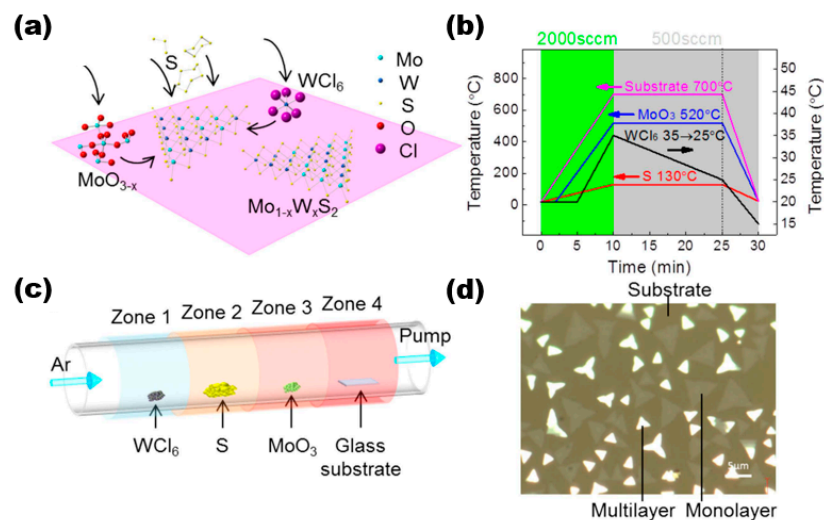
Figure 3. LP-CVD synthesis of monolayer $Mo_{1-x}W_xS_2$. (**a**) Schematic illustration of the surface reactions during CVD growth; (**b**) the arrangement of WCl_6, sulphur, MoO_3, and substrate in the CVD system. They were placed from upstream to downstream in four different furnace zones. The temperatures of each zone could be controlled independently. (**c**) Temperature profiles of the precursors and the substrate during CVD growth. The temperatures of each precursor and the substrate rose to their designated values within 10 min under 2000 sccm Ar flow rate. Then, the Ar flow was switched to 500 sccm for film growth. The temperature of the substrate, MoO_3, and S sources were kept constant while the temperature of WCl_6 gradually dropped from 35 to 25 °C in 15 min before cooling down. (**d**) Optical image showing that the triangular flakes grew on the glass substrate (dark regions). Brighter ones are the multilayers, and less bright ones are monolayers. Reproduced under the terms of the CC-BY 4.0 license [18]. Copyright 2016, The Authors, published by Springer Nature.

2.1.3. Physical Vapour Deposition

The PVD is one of the easiest means to prepare alloy materials. In 2015, $MoS_{2(1-x)}Se_{2x}$ alloy materials were prepared by using the PVD method by Feng et al. [20]. In contrast to the growth conditions previously designed [21], the researchers were able to effectively suppress the decomposition of $MoSe_2$ under high-temperature conditions by enhancing the experimental conditions. This was achieved by introducing Se, which was enriched during the reaction. The entire reaction process is illustrated in Figure 4a. The process was carried out by placing the selenium powder in the upstream zone of the tube furnace with the temperature set at 300 °C; then, the powders of MoS_2 and $MoSe_2$ were placed in the order shown in the figure and evaporated by a high temperature (about 950~965 °C). The SiO_2/Si substrate was placed in the precipitation zone with a lower temperature (about 600~770 °C) for the growth of the target sample material. Finally, large-size highly crystalline $MoS_{2(1-x)}Se_{2x}$ (x = 0.41~1.00) monolayer alloy samples of different components were achieved. Figure 4b shows the optical images of the prepared $MoS_{0.78}Se_{1.22}$ monolayer sample, whose atomic force microscopy (AFM) images were fingerprinted on the monolayer sample. Furthermore, an analysis was conducted on the Raman spectra and fluorescence spectra of the material, which can be observed in Figure 4e. Due to the interrelation between the fluorescence spectra and band gap engineering properties of 2D TMD materials, it is imperative to emphasise the significance of fluorescence spectra in this context. The team verified the link between the forbidden band width and the degree of alloying of the alloyed material by using fluorescence spectroscopy, and they succeeded in achieving an effective modulation of the band gap from 1.86 to 1.55 eV (Figure 4). A comparable technique was employed to effectively synthesise $Mo_{1-x}W_xSe_2$ [17]. This resulted in a modulation of the band gap width from 1.56 to 1.65 eV.

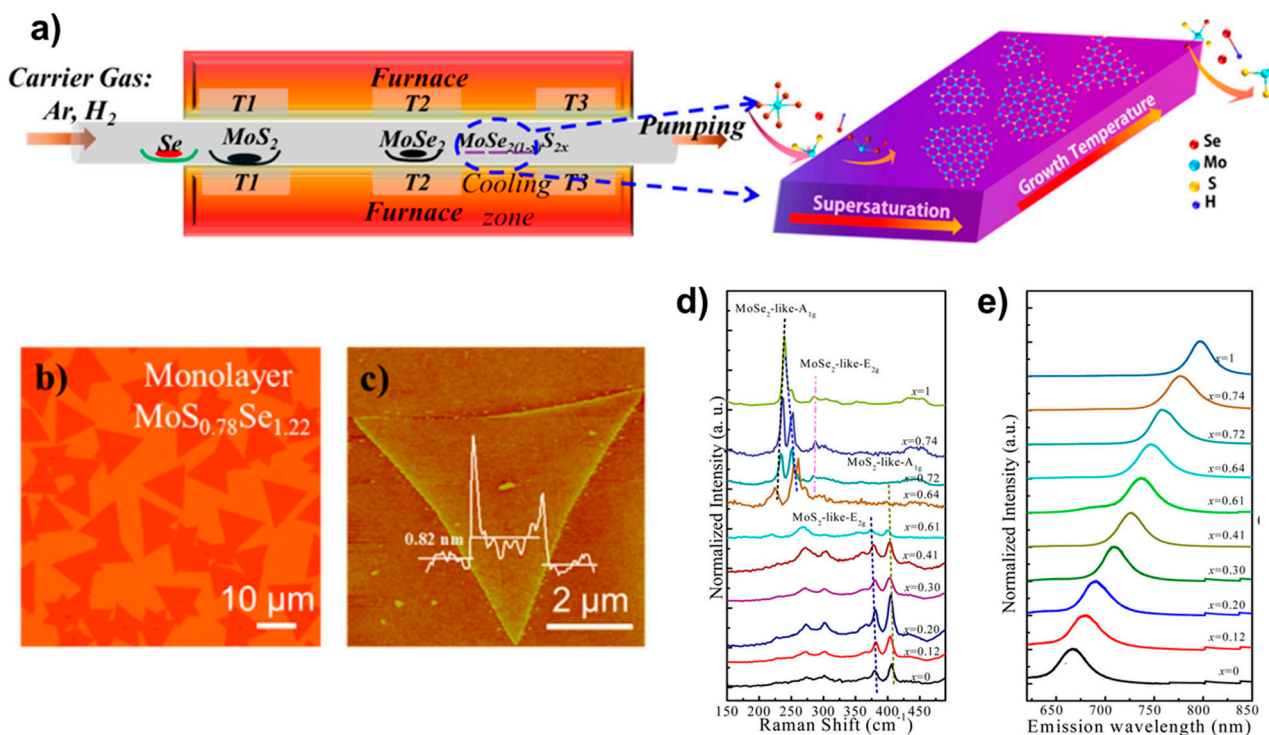**Figure 4.** (**a**) Illustration of monolayer $MoS_{2(1-x)}Se_{2x}$ growth. (**b**) Optical image, (**c**) AFM image, (**d**) the composition-dependent Raman spectra, and (**e**) the composition-dependent photoluminescence (PL) spectra. Reproduced with permission [20]. Copyright 2015, American Chemical Society.

The PVD method plays a crucial role in investigating the characteristics and uses of TMDs materials. However, the method's effectiveness is heavily dependent on the source material's properties, and there are limited controllable parameters throughout the synthesis process. Consequently, several materials cannot be synthesised successfully using this method, leading to a lower level of universality when compared to the CVD method. In contrast, the quality of samples produced through PVD is comparatively inferior to that of materials fabricated using the CVD technique. The constraints associated with PVD make it challenging to achieve widespread adoption in the realm of TMDs.

2.1.4. Molecular Beam Epitaxy (MBE)

The molecular beam is epitaxially grown on the substrate in the form of a scan, so it can be seen as a slow "stacking" of molecules into a crystalline material. In this method, the sample is grown layer by layer, so the growth rate is very slow, and the number of layers of material can then be controlled very carefully and precisely. Zhang et al. [22] conducted a related study using 2D $V_xMo_{1-x}Se_2$ prepared through molecular beam epitaxy. The MBE technique requires the material to be grown on a conductive substrate, which poses a limitation for in situ characterisation of the resulting samples. This is a well-known constraint of the MBE process. On the other hand, the growth conditions for sample preparation using the MBE method are very stringent and expensive, and the preparation on a large scale is influenced by the size of the cavity and substrate, so the MBE method is unsuitable for synthesising materials over large areas. Furthermore, the crystals produced through MBE are relatively diminutive, impeding the investigation of superior materials for practical purposes.

2.1.5. Atomic Layer Deposition (ALD)

In a paper published by Song et al. [23] in 2015 on the preparation of molybdenum disulphide tungsten alloy materials for controlled growth, they used ALD for the synthesis of the materials, and the schematic diagram of their overall preparation is shown

in Figure 5a. In this work, they first performed a hypercyclic atomic layer deposition preparation process constructed by n ALD cycles of MoO_x and m ALD cycles of WO_3, and the deposited $Mo_{1-x}W_xO_y$ alloy film samples were sulfidised. Different cycles were used for $MoO_x(n)$ and $WO_3(m)$ in one overall cycle to deposit 0.8–0.9 nm thick composition-controlled $Mo_{1-x}W_xO_y$ alloy films, which in turn led to the preparation of monolayer $Mo_{1-x}W_xS_2$ alloy samples (AFM images are shown in Figure 5b). They all exhibited good homogeneity and continuity. The thicknesses of $Mo_{0.2}W_{0.8}S_2$, $Mo_{0.4}W_{0.6}S_2$, and $Mo_{0.7}W_{0.3}S_2$ were all 0.1 nm, which corresponds to the monolayer $Mo_{1-x}W_xS_2$ alloys. Bilayer and trilayer $Mo_{1-x}W_xS_2$ samples were also successfully prepared by using this method. The study conducted an evaluation of the interlayer coupling effects on the interlayer transition process [24–27] in the synthesised multilayers of vertically composition-controlled $Mo_{1-x}W_xS_2$ materials. This evaluation was based on a comparison of the interlayer transitions of three different sample types, as illustrated in Figure 5c. Although these sample types are not particularly relevant to the paper, the study found that strong interlayer coupling effects were present.
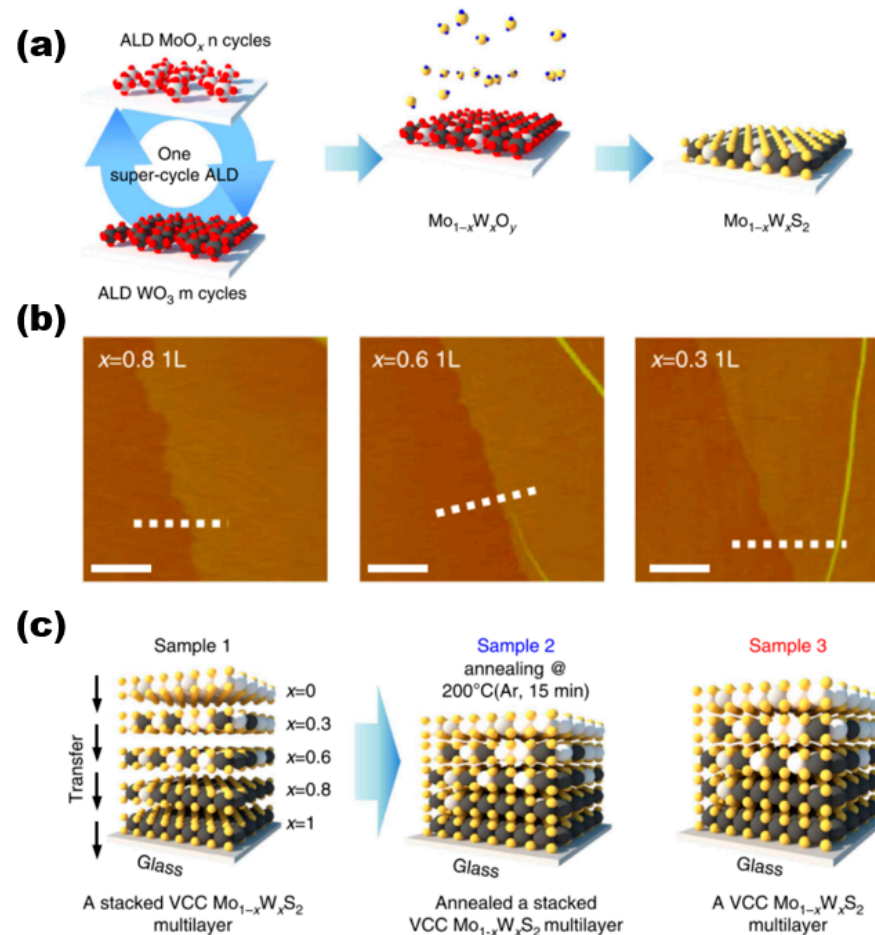

Figure 5. (**a**) Synthesis procedure of super-cycle ALD for $Mo_{1-x}W_xS_2$ alloy. (**b**) AFM images of composition-dependent molybdenum disulphide tungsten alloy materials. (**c**) Schematics of three sample types for ultraviolet–visible spectrophotometer measurement. Reproduced under the terms of the CC-BY 4.0 license [23]. Copyright 2015, The Authors, published by Springer Nature.

ALD is a method that produces high-quality crystals. However, the equipment required for this process is expensive and not universally applicable. Additionally, the deposition rate of the ALD method is slow, which limits its use and commercial industrial applications.

2.1.6. Chemical Vapour Transport

The CVT is a widely used synthesis technique in the laboratory for producing 2D alloy materials. CVT reactions involve a solid material that is not readily vapourised and can react with a gas-phase reactant to form a gaseous product. The gaseous product then deposits the crystalline material in the material growth zone. This gas-phase reactant is called a transport agent (Figure 6a) [28], which shows a typical synthesis of TMD crystals. To ensure successful reaction progression, it is imperative to regulate the temperature within both the reaction and growth zones. This necessitates the creation of a specific temperature gradient, which is crucial for the proper execution of the experiment. In the reaction zone, the solid (powder) and the transport agent react in the gas phase. then slowly diffuse into the growth zone, and deposit in its region, gradually forming the crystalline material (Figure 6b) [29]. It is worth noting that the formation process of bulk TMD crystalline materials is, as a rule, a heat absorption process, so the temperature T_1 (sublimation temperature) is set higher than T_2 (deposition temperature) in most cases. The CVT method is widely recognised as a dependable and effective means of producing bulk TMD crystalline materials for both scientific and commercial purposes.
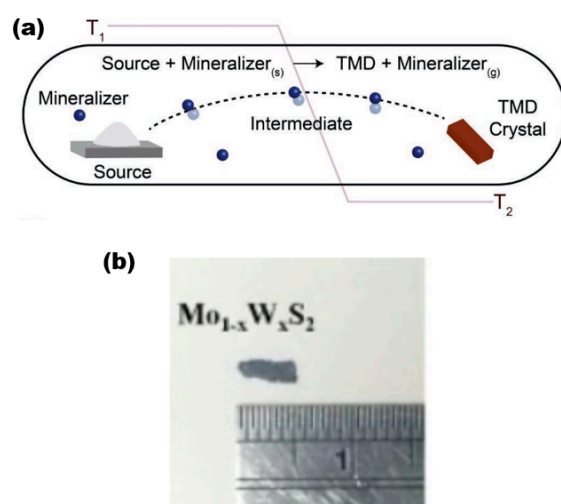

Figure 6. (**a**) Schematic diagram of the reaction process of the CVT method. Reproduced with permission [28]. Copyright 2019, Wiley-VCH. (**b**) $Mo_{1-x}W_xS_2$ sample pictures. Reproduced with permission [30]. Copyright 2017, IOP Publishing on behalf of the Japan Society of Applied Physics (JSAP).

The following is a discussion of the preparation process for $Mo_{1-x}W_xS_2$ single crystals using the CVT method [30] as an example. To prepare $Mo_{1-x}W_xS_2$ crystalline material, the solid reactants generally used are molybdenum powder (99.99% purity), tungsten powder (99.99%), and sulphur powder (99.999%), with iodine gas as a transport agent. The quartz tubes used were 20 cm × 22 mm × 17 mm in size (corresponding to tube length, outer diameter, and inner diameter, respectively), cooled in liquid nitrogen, evacuated to 10^{-6} Torr, and sealed. The tubes underwent pre-reaction at a temperature of 1000 °C for a duration of 2 weeks. Subsequently, they were subjected to a three-zone furnace with a temperature gradient ranging from 960 to 1050 °C. This was carried out to ensure that the growth conditions of the desired samples were met. Finally, after a growth cycle of about one month time, the furnace was slowly cooled down to room temperature. Finally, the large-size target sample was obtained in the growth zone (Figure 6b), and the size of the prepared crystalline $Mo_{1-x}W_xS_2$ sample was about 2 × 5 mm² with a thickness range of 3–6 μm.

The selection of the transport agent is a crucial factor in the advancement of the entire CVT method reaction process. Iodine gas, hydrogen halide, and hydrogen are commonly selected as transport carriers for most TMDs. The basis for their selection is closely related to the inherent stability of the solid reactants [31].

Mechanical stripping, CVD, PVD, MBE, ALD, and CVT mentioned above are all commonly used methods for the preparation of 2D TMDs alloy materials. It is worth noting that the specific details of the preparation process may vary significantly depending on the selected TMD alloy, synthesis method, and research objectives. The properties of the resulting materials are optimised by exploring different growth conditions and techniques for specific applications such as catalysis, electronics, or photonics.

2.2. Characterisation Methods for 2D TMDs Alloy Materials

The laboratory characterisation process for 2D alloy materials involves methods such as optical microscopy (OM), scanning electron microscopy (SEM), atomic force microscopy (AFM), X-ray diffraction (XRD), X-ray photoelectron spectroscopy (XPS), Raman spectroscopy, photoluminescence (PL) spectroscopy, and other similar techniques. These methods are used to determine the size, shape, thickness, and composition of the prepared 2D alloy materials, similar to traditional 2D material characterisation methods.

2.2.1. Morphological Structure Analysis

1. Optical microscope

The optical microscope enables the initial observation of the sample's distribution on the substrate and facilitates the easy and quick acquisition of information on the sample's shape and size. Figure 7a is a 2D material transfer system (with a metallographic optical microscope) of Nanjing Metatest corporation. The optical schematic diagram of the optical microscope is shown in Figure 7b.
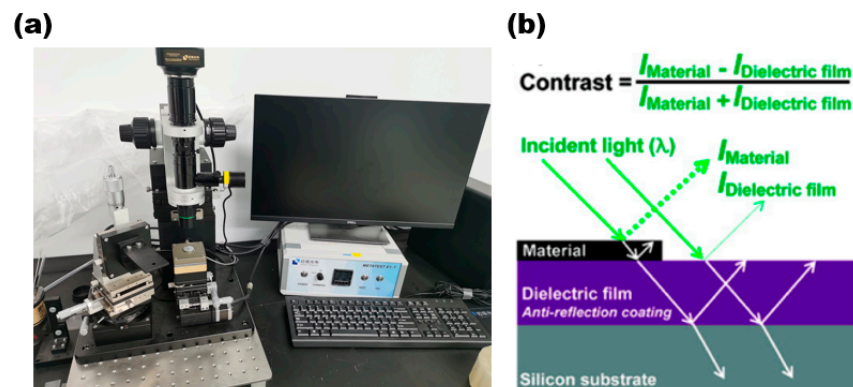

Figure 7. (**a**) Two-dimensional Transfer System with Optical Microscope; (**b**) optical schematic diagram of optical microscope. Reproduced with permission [32]. Copyright 2017, American Chemical Society.

Optical microscopy plays a crucial role in the initial examination of a sample microstructure and serves as a tool for characterising the underlying morphology. By utilising OM, we can obtain fundamental information about the sample surface, such as size and morphology. Figure 8 shows 2D optical photographs of materials taken by researchers using optical microscopy [19,33–35]. In Figure 8a are the ternary alloy materials MoS_xTe_{2-x}, $MoSe_xTe_{2-x}$, WS_xTe_{2-x}, WSe_xTe_{2-x}, NbS_xSe_{2-x}, $Mo_xN_{1-x}S_2$, $Mo_xNb_{1-x}Se_2$, $Mo_{1-x}Re_xS_2$, $W_xNb_{1-x}S_2$, $W_xNb_{1-x}Se_2$, and $Mo_xW_{1-x}Te_2$, the quaternary alloy $Mo_xNb_{1-x}S_{2y}Se_{2(1-y)}$, the quintuple alloy material $V_xW_yM_{1-x-y}S_{2z}Se_{2(1-z)}$, and the optical pictures of the 1T'-$MoTe_2$/2H-$MoTe_2$ and MoS_2-$NbSe_2$ heterostructures. The optical photographs presented herein depict the surface morphology of the bulk crystalline material. Figure 8b displays a photograph of a single crystal of MoS_2, showcasing a hexagonal spiral shape that is associated with the material growth mechanism. By examining the sample photographs captured via an optical microscope, one can obtain preliminary information regarding the sample's shape, size, and other characteristics. In addition, from the obvious optical contrast lining for few-layer materials, such as in the optical photograph of $SnSe_{0.5}S_{1.5}$ nanosheets in Figure 8c and the photograph of a single crystal of $SnSe_{0.5}S_{1.5}$ shown in the

inset, we can predict the thickness of the sample, i.e., the darker areas have a large thickness under the optical microscope, while the relatively brighter areas have a smaller thickness.
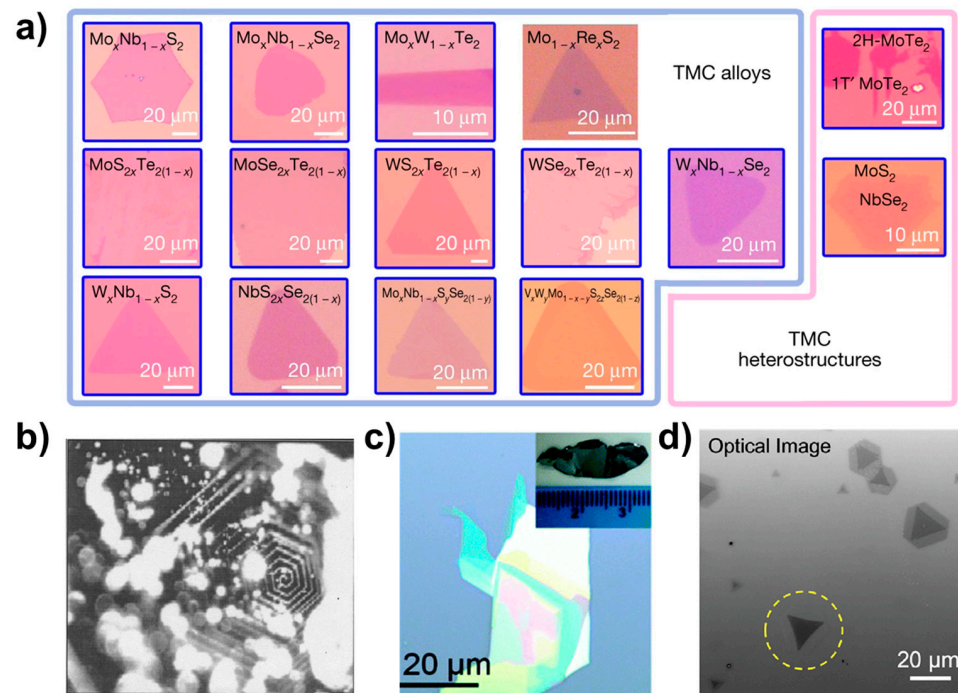

Figure 8. Optical images. (**a**) Optical photos of TMCs alloy materials and heterostructures. Reproduced with permission [19]. Copyright 2018, Springer Nature. (**b**) MoS_2. Reproduced with permission [33]. Copyright 2004, Indian Academy of Sciences. (**c**) $SnSe_{0.5}S_{1.5}$. Reproduced with permission [34]. Copyright 2017, Royal Society of Chemistry. (**d**) Optical image of MoS_2-WS_2 lateral heterostructures. The laser-irradiated flake is marked with a yellow dashed circle. Reproduced with permission [35]. Copyright 2021, American Chemical Society.

Figure 8d illustrates the heterogeneous structure of MoS_2-WS_2. The monolayer depicted in the figure displays a distinct optical contrast in the area highlighted by yellow circles as compared to other regions.

2. Atomic force microscopy

AFM has the capability to not only investigate the surface morphology of a sample but also to assess its mechanical characteristics, including hardness, elasticity, and plasticity. AFM has the characteristics of high accuracy, low damage to the sample, and wide range of use, making it widely used. In general, the working modes of AFM testing include contact, non-contact sub, and click type. This subsection presents AFM images of various 2D TMDs materials that are commonly used. The images are illustrated in Figure 9. The optical pictures and AFM images of the $Mo_{1-x}W_xS_2$ monolayer alloy studied by Chen et al. [36] are shown in Figure 9a, where the layers of the alloy film sample were identified using AFM measurements. This included one layer, two layers, and the thickness of the monolayer alloy sample of approximately 1.0 nm (inset in a). Figure 9b,c show AFM images of $MoS_{1.60}Se_{0.40}$ monolayer semiconductor alloys [37] and AFM images of MoS_2/WS_2 heterostructures with a thickness of about 0.8 nm, respectively [38]. The formation mechanism of helical WS_2 [37] was probed by Fan et al., and the AFM images they constructed are presented in Figure 9d–i. The central region of Figure 9d reveals an obvious triangular helical morphology after the magnification of Figure 9e The AFM of the magnified Figure 9c, focusing on its edge dark region, indicates that the heights of these steps are approximately 0.7 nm, 0.9 nm, 3.6 nm, and 3.8 nm, and the growth process of the AFM image with such a representative helical dislocation, i.e., terminated at the central/eccentric position, was investigated based on the AFM images (Figure 9h,i marked with red lines).
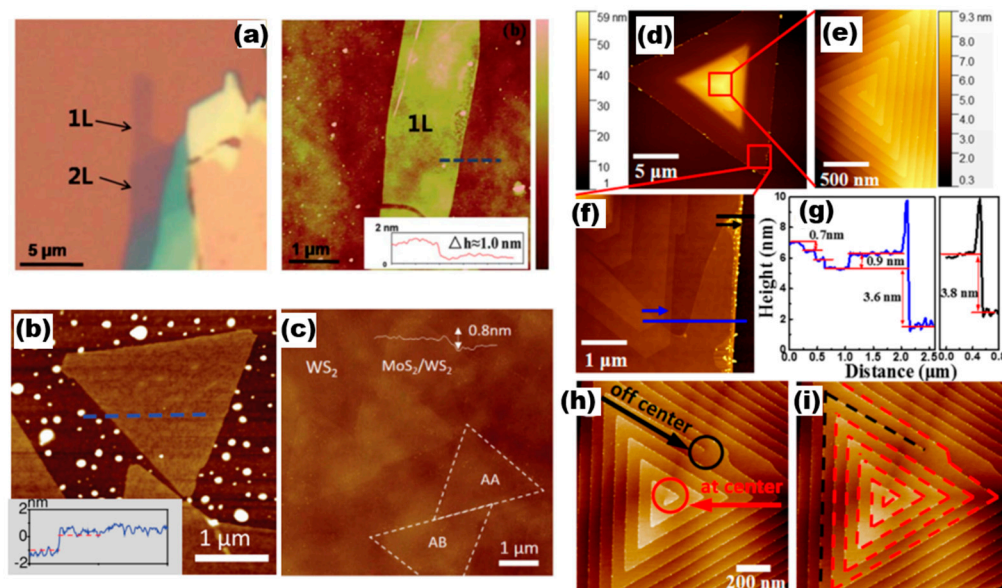
Figure 9. AFM images with the line profiles. (**a**) Optical micrograph and AFM of $Mo_{0.47}W_{0.53}S_2$ flake. Reproduced with permission [36]. Copyright 2014, Royal Society of Chemistry. (**b**) AFM image of $MoS_{1.60}Se_{0.40}$. Reproduced with permission [21]. Copyright 2014, Wiley-VCH. (**c**) AFM image of MoS_2/WS_2. Reproduced with permission [38]. Copyright 2016, Wiley-VCH. (**d–i**) AFM image of WS_2 a single spiral structure. Reproduced with permission [37]. Copyright 2018, American Chemical Society.

AFM is capable of providing clearer and more intuitive sample information compared to optical microscopy. It boasts a highly sensitive surface-state-sensing capability, allowing for the probing of material surface information with exceptional clarity and rapid precision. It brings convenience to studying the thickness of 2D alloy materials. Meanwhile, compared with the STM characterisation method, AFM requires a smaller operating environment and is not affected by the sample conductivity. Based on these advantages, AFM has been widely used [39]. AFM has made significant advances in characterising Fermi levels and hidden interfaces in materials, with techniques such as scanning Kelvin probe force microscopy (SKPFM) [40–42], Kelvin probe force microscopy (KPFM) in ultrahigh vacuum [43,44], etc., which have enabled researchers to probe electronic properties and surface structures at the nanoscale.

3. Scanning Electron Microscopy

The scanning electron microscopy (SEM) offers the benefit of a wider scanning field of view and the capability to focus on samples ranging from the nanometre to the millimetre scale. The SEM provides more comprehensive sample information compared to optical microscopy. It can observe the geometry, dispersion state (powder), particle size, and distribution of the sample being measured. Additionally, it can determine the elemental composition or phase structure of a specific morphology in a specific region. This information is not available through optical microscopy [45]. In conclusion, the comprehensive nature of SEM presents a promising future for the investigation of the physical properties of materials.

The SEM images of the synthesised $MoS_{1.5}Se_{0.5}$ and $WS_{1.62}Se_{0.38}$ ternary alloy samples are presented in Figure 10. The images depict the samples at low and high magnification [45]. It can be clearly seen that both $MoS_{1.5}Se_{0.5}$ and $WS_{1.62}Se_{0.38}$ show layered features and have the same structure, i.e., they are composed of hexagonal nanoflakes with smooth surfaces. The pyramidal helical structure of MoS_2 is fully visible in Figure 10e, with the clockwise growth direction indicated by the white arrow. The SEM in Figure 10f shows that we can observe the different "steps" in the formation of the "pyramid" configuration, which are marked in the figure, and the edge areas are defects of the sample, which lead to

the deviation of the sample from the standard perfect triangle. The SEM is a useful tool for analysing samples, providing information on their structural characteristics, surface dimensions, and crystallinity. Additionally, the SEM can be used to study the distribution of elements in specific micro-regions, determine the percentage of each element present, and gather other relevant data. This information is particularly valuable for investigating the structure, growth mode, and properties of 2D materials. It is involved in the examination of the configuration, development pattern, and characteristics of 2D substances.
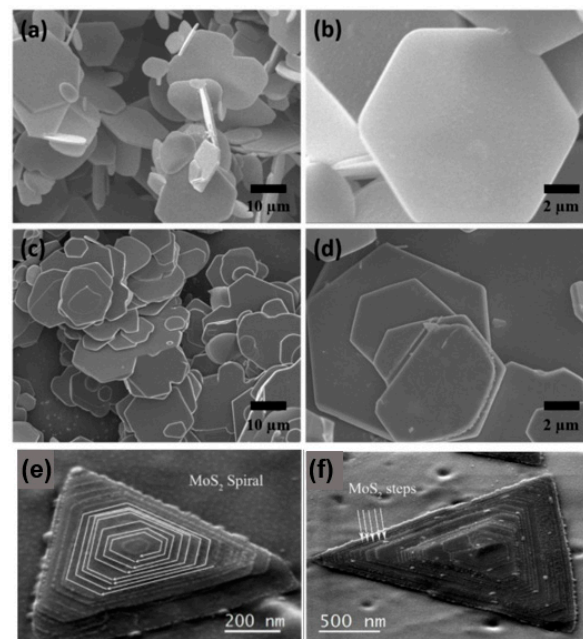

Figure 10. SEM images. (**a**) Low magnification and (**b**) high magnification SEM images of $MoS_{1.5}Se_{0.5}$. (**c**) Low magnification and (**d**) high magnification SEM images of $WS_{1.62}Se_{0.38}$; (**e**) SEM image of MoS_2; and (**f**) SEM image of a MoS_2 showing the multiple layered steps. (**a**–**d**) Reproduced with permission [45]. Copyright 2017, Elsevier. (**e**,**f**) Reproduced with permission [46]. Copyright 2017, Springer Nature.

2.2.2. Optical Characterisation

1. Raman spectroscopy

The Raman effect, also known as Raman scattering, was first observed by Chandrasekhara Venkata Raman, an Indian physicist, in 1928. In recognition of his contributions to the field of optics, he was awarded the Nobel Prize in Physics in 1930.

Raman spectroscopy is a convenient and fast technique to study the properties of 2D TMDs materials because of its ease of operation, fast measurement, low maintenance cost, high resolution, lack of contact and damage to the sample, the ability to test at low temperatures and high pressures, accurate imaging, and the ability to provide information on the lattice structure and electronic structure of the measured sample. The Raman characteristic peaks of 2D materials are affected by their coupling properties, resulting in their appearance or shift. At wave numbers below 50 cm^{-1}, the phonon shear mode (SM) and layer breath mode (LBM) can be directly observed. This technique has also been widely applied to study the stacking behaviour of 2D van der Waals heterojunctions [47]. Zhang et al. [38] have identified new phonon modes, SM and LBM, in a stacked configuration of bilayer heterostructures such as MoS_2/WS_2. These modes are observed in structures with strong interlayer coupling forces and correspond to relative and mutual vertical oscillations of the rigidity between adjacent layers of a bilayer heterogeneous structure. Figure 11a illustrates these modes, where SM and LBM represent the former and the latter, respectively. The interaction between these modes can be likened to a "spring" connecting two sulphur layers. These phonon modes are particularly important for investigating the

thickness of the sample layers, the way the samples are stacked, the surface adsorption, and the contact quality of the 2D material hybridisation. Figure 11e presents the low-wavenumber Raman spectra of MoS_2 films on WS_2, AA stacking mode, AB stacking mode, and corner heterojunctions. It can be clearly seen that the Raman shift of the A-B stacked LBM is increased by 2 cm^{-1} compared to the A-A stacked bilayer structure, which can be attributed to the shorter interlayer distance and stronger interlayer coupling force of the A-B stacked approach. It can also be seen that the LBM vibration frequency of the corner heterojunction MoS_2/WS_2 is significantly lower by 2–4 cm^{-1} compared to that of the A-B stacked MoS_2/WS_2, which indicates weaker interlayer coupling and lower stacking efficiency.
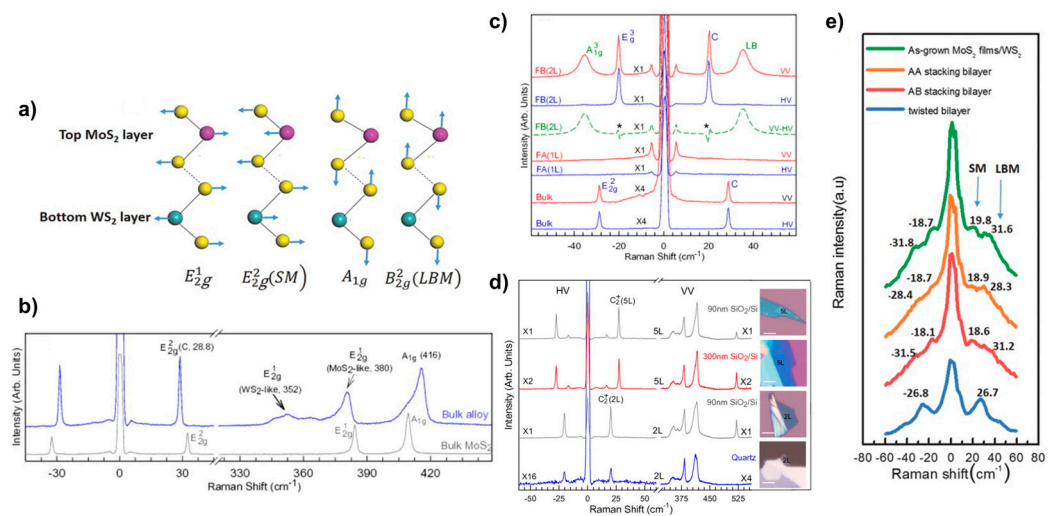

Figure 11. (**a**) Schematic diagram of lattice structure and vibrational mode for bilayer heterostructure WS_2/MoS_2. (**b**) Raman Spectra of Bulk $MoWS_2$ and MoS_2; (**c**) low-wavenumber Raman in Polarised Mode of bulk, 1L, and 2L alloy flake $MoWS_2$; (**d**) polarisation Raman spectra of few-layer $MoWS_2$ on different substrates; and (**e**) low-frequency Raman spectroscopy of layer breath mode and shear mode. (**a**,**e**) Reproduced with permission [38]. Copyright 2016, Wiley-VCH. (**b**–**d**) Reproduced with permission [48]. Copyright 2015, AIP Publishing.

Moreover, the interconnection of individual monolayers in 2D materials is facilitated by van der Waals interaction forces. The characteristics of multilayer alloys, on the other hand, are dependent on the number of layers they possess. Qiao et al. [48] conducted a study on the linkage between the number of layers of an alloy and its sheer mode and layer breathing mode. As shown in Figure 11b, the Raman peak at 416 cm^{-1} is designated as A_{1g} due to the spatial point group type D6h of the bulk alloy, which is located between MoS_2 (409 cm^{-1}) and WS_2 (420 cm^{-1}) [49]. In contrast, the MoS_2-like and WS_2-like alloys, E_{2g}^1, are represented at 380 cm^{-1} and 352 cm^{-1} Raman shifts, respectively, and an ultralow-frequency (ULF) Raman peak is observed at 28.8 cm^{-1}. The SM mode in the bulk alloy is responsible for this attribute. Figure 11c demonstrates the observation of the ULF peak under polarisation. The FWHM in the bulk alloy is approximately 1.1 cm^{-1}, which is consistent with the bulk MoS_2.

The above studies have shown that LBM and SM vibrations in low-wavelength-number Raman spectroscopy can be used as a fingerprint characterisation of stacking configurations of 2D materials. There is also a large body of work on Raman studies of $Mo_{1-x}W_xS_2$ 2D alloy materials doped with X [36] and at different temperatures [50].

2.   Photoluminescence spectra

When a high-density energy laser beam is directed onto the surface of a sample, it results in the occurrence of the PL phenomenon. PL spectroscopy is a highly precise method for evaluating the photoelectric characteristics of semiconductor materials. It is a non-

invasive testing technique that does not damage the sample, making it a valuable tool in both the semiconductor industry and research domains. The fluorescence spectrum of light exhibits varying wavelengths across different semiconductor materials, thereby serving as a direct indicator of the sample's structure and composition. Furthermore, as previously stated, the energy band structure and forbidden band width of ternary semiconductor alloy materials vary with changes in their components. Therefore, the proportion of components can be identified by examining the forbidden band width through PL testing. The PL spectra of various monolayer 2D alloy materials are presented in Figure 12. The spectra demonstrate the variation of component content and reveal that continuous adjustment can be achieved within the ranges of 670–800 nm, 620–680 nm, and 760–780 nm. That is, in the content variation range of $MoS_{2(1-x)}Se_{2x}$ from x = 0 to x = 1, the PL peak position underwent a continuous red-shift phenomenon, and the band gap opening became smaller and smaller. In contrast, the PL peaks of $Mo_{1-x}W_xS_2$ and $Mo_{1-x}W_xSe_2$ continued to blue-shift as the content of the components became larger, indicating that the forbidden band widths became larger as the component x increased. In summary, the application of PL spectroscopy can be utilised to acquire data on the forbidden band width of a sample. This information can be further examined in the area of regulated band gap engineering. In addition to PL spectroscopy, stoichiometry can be determined by using XRD, energy-dispersive X-ray spectroscopy (EDS), electron energy loss spectroscopy (EELS), XPS, chemical analysis, and other methods.
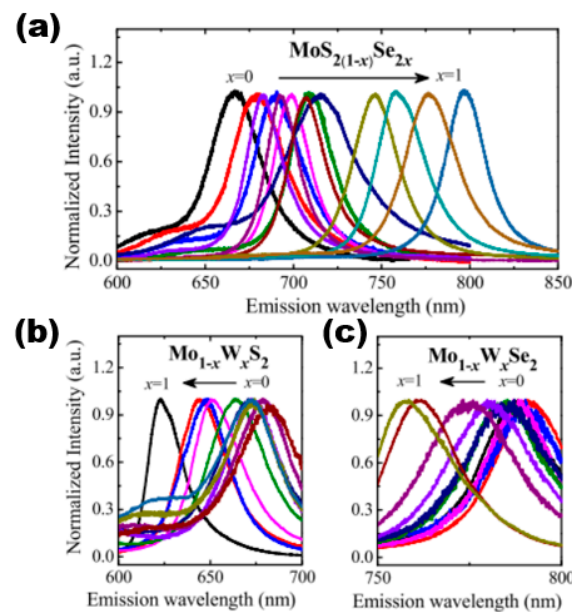

Figure 12. Composition-dependent PL spectra of (**a**) $MoS_{2(1-x)}Se_{2x}$ monolayers, (**b**) $Mo_{1-x}W_xS_2$ monolayers, and (**c**) $Mo_{1-x}W_xSe_2$ monolayers in the whole composition range (x = 0–1). Reproduced with permission [51]. Copyright 2015, The Royal Society of Chemistry.

3. Photovoltaic Properties and Applications of 2D TMDs Alloy Materials

The precise regulation of energy bands in 2D semiconductor materials is necessary to fulfil the requirements of multifunctional materials in the optoelectronics field. Alloying engineering offers the advantage of continuously adjusting band edges, band gaps, and lattice constants, making it a popular area of interest among researchers. Transition metal materials within the same subgroup tend to form alloys and other compounds due to their similar lattice symmetry and low degree of lattice mismatch. As a result, a variety of transition metal sulphide compound alloy materials, such as $Mo_{1-x}W_xS_2$ and $Mo_{1-x}W_xSe_2$, have been extensively studied and reported. This section provides a comprehensive analysis of the development of 2D TMDs alloy materials. It covers a range of topics, including optoelectronic properties and their applications in hydrogen evolution reaction catalysis,

field-effect transistors, lithium-sulphur battery catalysts, lasers, and other fields. The discussion is presented in a systematic manner.

3.1. Optoelectronic Properties of 2D TMDs Alloy Materials

The single-layer 2H phase MoS_2 and WS_2 are direct band gap semiconductor materials that emit light at approximately 650 nm and 590 nm bands, respectively. The single-layer MoS_2 is suitable for direct application in field-effect transistors. The structure and properties of WS_2 and MoS_2 are similar, enabling them to form an alloy phase easily. However, current scientific research on $Mo_{1-x}W_xS_2$ is limited. The present scientific research on $Mo_{1-x}W_xS_2$ primarily concentrates on the development and adjustable band gap efficiency of single-layer or few-layer alloys. In terms of alloy growth, since the earliest 2D alloy is generally obtained by mechanical stripping [52–54], monolayer samples of 2D alloy materials were also obtained by mechanical stripping [16], but the stripped samples were too small in size and wasted, after which researchers obtained monolayer samples by using CVD, CVT, and ALD to prepare large-area, high-quality $Mo_{1-x}W_xS_2$ 2D alloys with gradient layer structures [18,23]. Figure 13 shows the band structures of $MoS_{2(1-x)}Se_{2x}$ and $Mo_{1-x}W_xS_2$ [55].
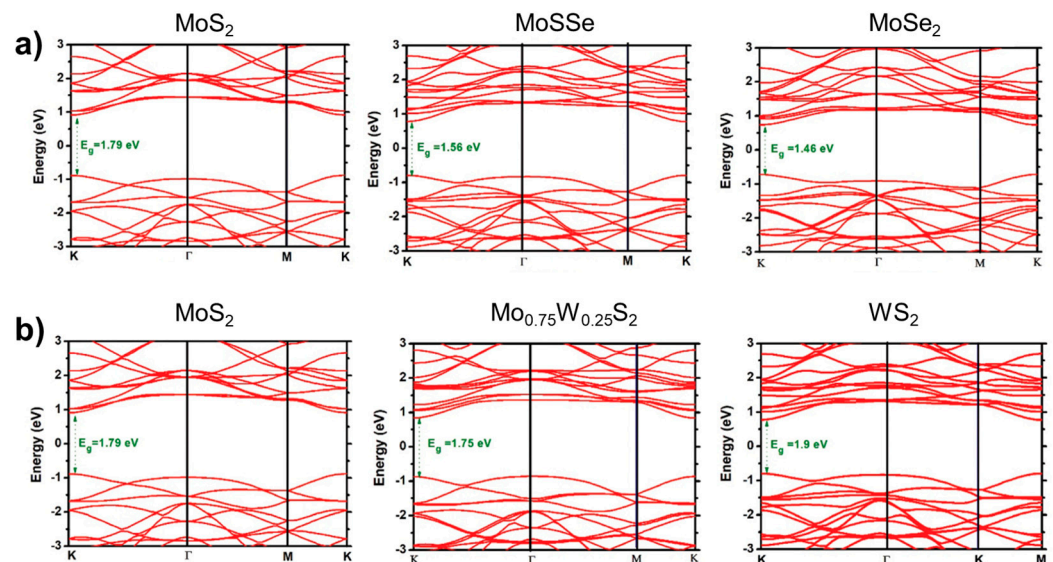

Figure 13. Band structures are shown for the TMD-ML alloys. (**a**) $MoS_{2(1-x)}Se_{2x}$ with x = 0.0, 0.5, and 1.0 and (**b**) $Mo_{1-x}W_xS_2$ with x = 0.0, 0.25, and 1.0. Reproduced under the terms of the CC-BY 4.0 license [55]. Copyright 2021, The Author(s). Published by IOP Publishing Ltd. on behalf of the Institute of Physics and Deutsche Physikalische Gesellschaft.

During the characterisation process of the 2D alloy material, the AFM was used to determine that the thickness of the monolayer $Mo_{1-x}W_xS_2$ alloy material was approximately 0.7 nm. Additionally, the SEM detected a consistent distribution of elements on the surface of the monolayer alloy material. The SEM also observed a uniform distribution of elements on the surface of the monolayer alloy material; Raman spectroscopy showed the presence of two characteristic modes, MoS_2-like E' and WS_2-like E', as well as the A' mode, which was blue-shifted with increasing tungsten (W) fraction because the A' mode is only related to the vibrations of sulphur (S) atoms, while the E' mode exhibits a bimodal behaviour attributed to the combined vibrations of the metal and S atoms [36,56]. The atomic structure (ordered, disordered, or clustered) of the material was observed using scanning transmission electron microscopy (STEM), and it was found to have a disordered distribution [57]. The PL spectra exhibited two distinct peaks, namely the A and B peaks. These peaks demonstrated a red-shift followed by a blue-shift in energy as the W component increased. The energy range of these peaks varied between 1.8 eV–2 eV and 2 eV–2.4 eV. Additionally, the energy band bending factors for the A and B peaks were 0.25 eV and 0.19 eV, respectively, as

reported in [16]. In contrast, for the laminar gradient alloys, the absorption spectra showed a wide absorption range of 1.2 eV–2.5 eV. Laminar gradient alloys exhibited favourable optoelectronic characteristics, producing a photocurrent that is 3–4 times greater than that of unalloyed 2D materials [23]. Stability analysis of the monolayer $Mo_{1-x}W_xS_2$ alloy material was performed theoretically using density flooding theory [58], which yielded negative formation energies and thus determined that the $Mo_{1-x}W_xS_2$ alloy is stable under general conditions. Also, they predicted the existence of two ordered phases ($x = 1/3$, $x = 2/3$) in the monolayer $Mo_{1-x}W_xS_2$ alloy.

3.2. Phase Changes

In addition to stable phases, TMDs have a number of substable phases with unique optical and electrical properties. By realising controlled phase transitions between different crystalline phases, TMDs exhibit some superior properties and new potentials in electronic and optoelectronic applications [59]. Wang et al. reported a CVD synthesis method. They synthesised monolayer $WS_{2(1-x)}Te_{2x}$ alloys with different Te ratios by modulating H_2 gas. A structural phase transition from the semiconducting 2H phase to the semi-metallic 1T′ phase at high Te ratios was achieved, and the optical band gap was red-shifted from 1.97 eV to 1.67 eV. The conductive behaviour of the device was effectively modulated (Figure 14) [60]. Zhang et al. achieved a 2H to 1T phase transition of $MoS_{2x}Se_{2(1-x)}$ and $Mo_xW_{1-x}S_2$ through Li-ion intercalation [61]. In addition, Amey Apte et al. achieved the 2H to 1T phase transition by applying stress to a $MoWSe_2$ alloy and verified the process using molecular dynamics simulations and in situ electron beam exposure with high-angle annular dark-field (HAADF) STEM imaging [62].
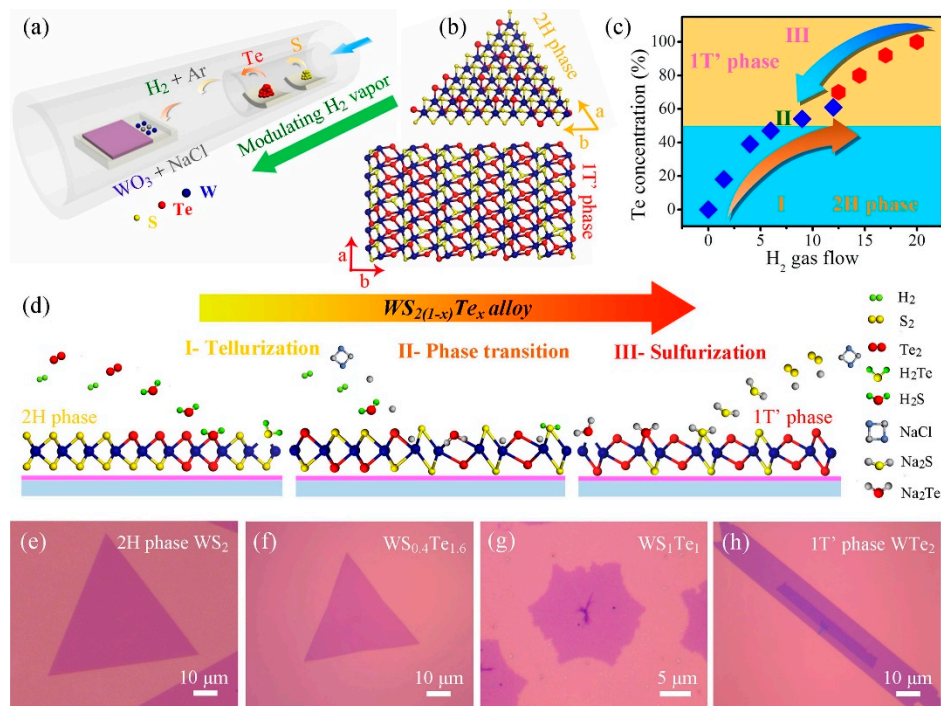
Figure 14. (**a**) Schematic illustration of the $WS_{2(1-x)}Te_{2x}$ CVD system. (**b**) Crystal structures of 2H and 1T′ phase $WS_{2(1-x)}Te_{2x}$ alloys, showing the distinguishing atomic configurations. (**c**) Summary of the Te concentration and the phase evolution as a function of the amount of H_2 gas flow. (**d**) Growth schematic for preparing 2H and 1T′ phase $WS_{2(1-x)}Te_{2x}$ alloys in our work. Part I and III: the evolutions of the telluriding (or sulphuring) process by increasing (or decreasing) the H_2 environment. Part II: the phase conversion from 2H to 1T′ phase with the increase in H_2 gas. (**e**–**h**) OM images of 2H phase WS_2, $WS_{0.4}Te_{1.6}$, 1T′ phase WS_1Te_1 and WTe_2 domains, respectively. Reproduced with permission [60]. Copyright 2019, Elsevier.

Phase transitions achieved by using electric field guidance were reported by Zhang et al. Structural transitions from 2H semiconductors to distorted transient structures (2Hd) and rhombohedral crystal Td conducting phases were achieved for resistive random-access memory (RRAM) devices based on 2H-MoTe$_2$ and Mo$_{1-x}$W$_x$Te$_2$. It was shown that controlled electrical state switching in 2D materials is achievable [63].

3.3. Application of 2D TMDs Alloy Materials

Alloyed 2D materials possess adjustable properties and optoelectronic characteristics that surpass or are absent in the original 2D materials, as indicated in the above review. This subsection provides a brief introduction to the application of hydrogen precipitation catalysis and field-effect transistor devices.

3.3.1. Hydrogen Evolution Reaction (HER)

The production of clean energy (hydrogen) relies heavily on the development of stable and efficient HER catalysts. TMDs have gained significant attention in the field of photoelectrochemical (PEC) water decomposition due to their unique electronic and optical properties. These materials hold promise for efficient and sustainable hydrogen production through sunlight-driven water splitting, which is a crucial step in renewable energy generation and storage [64–68]. The HER is a crucial half-reaction in electrochemical and photoelectrochemical water-splitting processes. The electroactivity of TMDs can be modulated by changing their electronic structure, and the HER activity is dependent on the proportion of the alloy.

Zhu et al. achieved excellent catalytic activity, long-term stability, and universality based on MoS$_2$ under both acidic and alkaline conditions [69]. 1T′-WTe$_2$ nanoribbons have also been reported to exhibit ultrahigh stability over 5000 cycles and 20 h at 10 mA/cm^2 current [70]. The long-term stability of TMD alloy materials has also been demonstrated. The VSSe sample reported by Hu et al. exhibited a lower overpotential of -180 mV at a current density of 10 mA cm^{-2}, a Tafel slope of 87 mV dec^{-1}, and better durability [71]. Furthermore, the conductivity of the catalyst material is a critical factor in determining its catalytic performance. Among the reported MoS$_{2(1-x)}$Se$_{2x}$ [15] alloy materials, Figure 15a represents a linear scanning voltammogram of MoS$_{2(1-x)}$Se$_{2x}$, where the red line represents MoS$_2$ (x = 0), the blue line represents MoSe$_2$ (x = 1), the black line represents MoS$_{1.0}$Se$_{1.0}$ (x = 0.5), and the green colour represents Pt-C. The electrochemical activity exhibits diversity as the components vary. The data clearly show the positive effect of Se in the MoS$_2$ lattice or S in the MoSe$_2$ lattice on HER. Upon analysing the HER onset potential shift of few-layer MoS$_{1.0}$Se$_{1.0}$ in comparison to the few-layer MoS$_2$ and MoSe$_2$ nanosheets, it was observed that the alloyed material consistently outperforms the pure sulphide and selenide variants. Notably, MoS$_{1.0}$Se$_{1.0}$ exhibited the highest efficacy among all combinations. Moreover, the Tafel slope, a parameter used to evaluate the HER electroactivity and mechanism, was determined from the linear region of the data shown in Figure 15b, and it can be seen that the Tafel slope is 96 mV dec^{-1} for MoSe$_2$, 95 mV dec^{-1} for MoSe$_2$, and about 56 mV dec^{-1} for MoS$_{1.0}$Se$_{1.0}$. For a constant load of 180 µg cm^{-2}, the exchange currents obtained from the polarisation curves were 320 µA cm^{-2} for MoS$_{1.0}$Se$_{1.0}$, 45 µA cm^{-2} for MoSe$_2$, and 36 µA cm^{-2} for MoS$_2$, indicating the highest HER activity of MoS$_{1.0}$Se$_{1.0}$ compared to MoSe$_2$ and MoS$_2$. The collective findings indicate that effective doping of materials results in a significant increase in their HER activity. Additionally, modifying the composition of layered sulphide generics to fine-tune their electrochemical activity positively impacts the photocatalytic hydrogen precipitation on 2D materials.
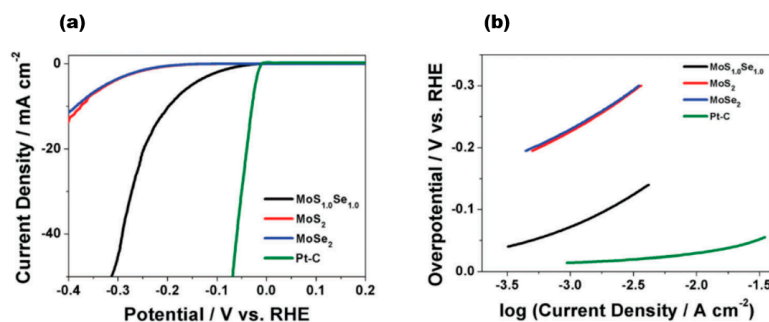
Figure 15. (**a**) IR-corrected linear sweep voltammograms of $MoS_{2(1-x)}Se_{2x}$; (**b**) Tafel plots corresponding to $MoS_{2(1-x)}Se_{2x}$ and Pt–C. Reproduced with permission [15]. Copyright 2014, Royal Society of Chemistry.

Kang et al. synthesised alloy nanosheets of $Re_{1-x}Mo_xSe_2$ (x ranging from 0 to 100%) by using a hydrothermal reaction. A phase transition evolution process of 1T″->1T′->2H occurred as x increases. Their results showed that the HER catalytic activity depends on x, with the best catalytic activity at x = 10% [72]. They synthesised $(MoWV)Se_2$ nanosheets with different compositions by using another colloidal reaction in 2023, with the molar fraction of V atoms (X_V) increased to 0.8, which succeeded in generating a highly hydration-resistant metallic phase. And the phase transition from 2H to 1T occurred when the X_V value was in the range of 0.62–0.75. They demonstrated that the HER properties improve with the increase in X_V [73].

3.3.2. Field-Effect Transistor (FET)

Alloyed 2D TMDs materials exhibit more unique electrical properties than 2D TMDs. Liu et al. [74] successfully synthesised $Nb_xW_{1-x}S_2$ alloy materials and constructed field-effect transistor devices based on the alloy materials. The electrical measurements conducted indicated that the addition of Nb atoms to WS_2 resulted in the manifestation of P-type semiconductor characteristics. The incorporation of Nb dopants could effectively modulate the band gap of $Nb_xW_{1-x}S_2$ and enhance the optical properties of WS_2. The carrier type of WS_2 underwent a transition from intrinsic n-type to p-type upon Nb doping, which was a significant observation. Figure 16a shows the schematic diagram of the $Nb_xW_{1-x}S_2$-based FET device. The electrical transport characteristics of WS_2 and $Nb_xW_{1-x}S_2$ FETs were obtained by using electron beam lithography and vapour deposition of the sample with Ti/Au (10/30 nm) contacts and measured, and the inset shows the optical image of the $Nb_xW_{1-x}S_2$ FET device. The non-linear output of monolayer WS_2 was dependent on the source drain current (I_{ds}) and the n-type gate voltage (V_g), indicating the existence of a Schottky barrier between the Ti-WS_2 contacts. And the Ids showed a decreasing trend with increasing V_g after Nb doping, which indicated that $Nb_xW_{1-x}S_2$ is heavily p-type-doped. The Ids stayed at a high value and did not saturate when V_g was adjusted, indicating a better Nb doping effect. And this phenomenon can be explained by the tunnelling transport mechanism [75,76]. The rise in conductive current observed in $Nb_xW_{1-x}S_2$ can be attributed to the increase in hole concentration resulting from the doping process. This increase in hole concentration leads to a linear increase in Ids with V_{ds}, as illustrated in Figure 16c, when Nb is used as the dopant.
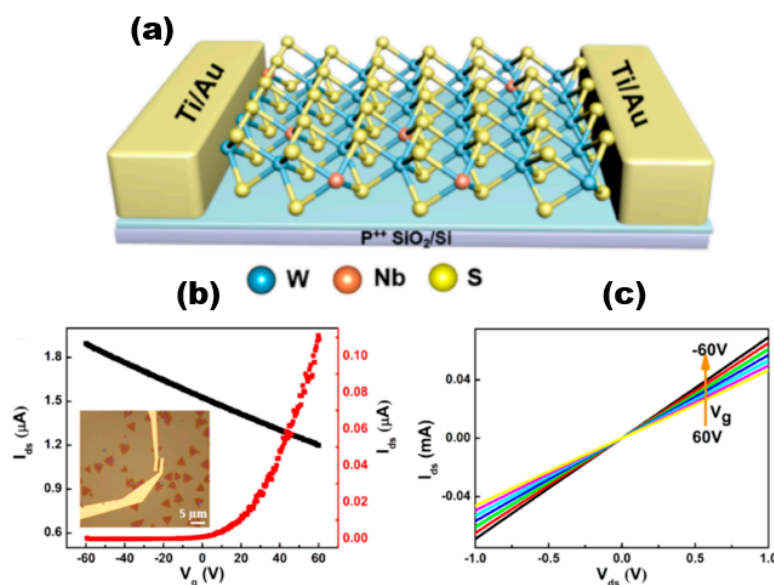
Figure 16. (**a**) Schematic of FET based on monolayer $Nb_xW_{1-x}S_2$; (**b**) I_{ds} and V_g characteristics of single-layer WS_2 and $Nb_xW_{1-x}S_2$ FET devices at different V_{ds}. (**c**) Current output curves of single-layer $Nb_xW_{1-x}S_2$ at different voltage values. Reproduced with permission [74]. Copyright 2019, American Chemical Society.

3.3.3. Lithium-Sulphur Battery Catalysts

As one of the most promising next-generation energy storage systems, lithium-sulphur batteries have the advantages of high theoretical energy density, higher energy density, abundant resources, and high safety [77,78]. However, their practical applications are limited by the growth of lithium dendrites and lithium polysulphide shuttles. In order to solve LiPS-related conversion problems, catalyst materials such as transition metal oxides, sulphides, nitrides, carbides, etc., are needed. TMDs, as relatively stable catalyst materials, can avoid side reactions in the battery cycle and improve the conversion of LiPSs. Bhoyate et al. in 2020 showed that LiPSs can be converted to LiPSs through a two-step process of co-sputtering and sulphurisation to synthesise a 2D $Mo_{0.5}W_{0.5}S_2$ alloy with 2H (semiconducting)-1T (metallic) mixed phase and confirmed the higher LiPS binding effect and catalytic performance by using electrochemical analysis [11]. They further synthesised the mixed 2H + 1T phase 2D MoWS alloy catalysts in 2021 by using the method of hydrothermal synthesis and defects engineering, which resulted in a high charge transfer and LiPSs conversion. The D-MoWS catalysts deposited on CNF paper maintained structural homogeneity during the etching process (Figure 17). The LSB anode with high sulphur loading (10 mg cm^{-2}) presented a high area capacity of 7.6 mAh cm^{-2}, high cycling stability (100 cycles), and a low N/P ratio (1.7) at 0.3C. By comparing the battery performance (within 10 cycles) of the bare CNF-S cathode with the same sulphur loading of 10 cm^{-2}, it was demonstrated that the catalyst efficiently utilises sulphur and reduces the N/P ratio, significantly increasing the weight energy density up to the highest reported value of 1090 Wh kg^{-1} [11]. Feng et al. used MoWS$_2$@MXene@CNT composite material as the main cathode material for L-S batteries, in which MoWS$_2$ acted as a polar substance to accelerate polysulphide conversion, MXene enhanced the electron conductivity, and CNT accelerated the electron transfer rate. The composite material showed good multiplicity and cycling stability as an electrode material [12].
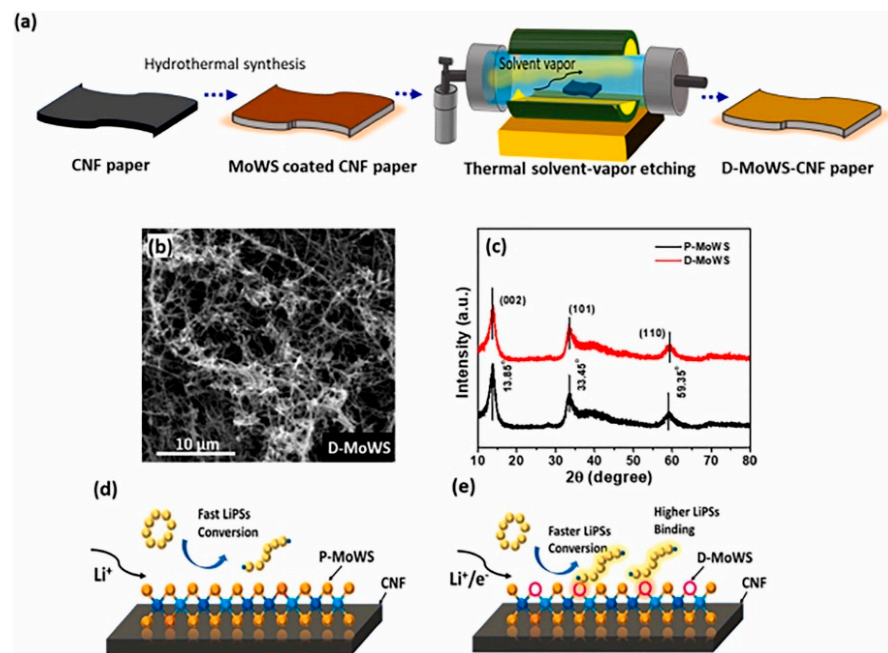
Figure 17. (**a**) Schematics illustrating the synthesis process of hydrothermally grown MoWS catalyst on CNF paper and its defect engineering process. Low-magnification FESEM image of (**b**) defect-engineered (D-MoWS) catalysts on CNF paper. (**c**) XRD analysis of P- and D-MoWS catalyst on CNF. (**d**,**e**) A schematic of P- and D-MoWS-CNF structure representing the effect of defect engineering on polysulphide binding and conversion. Reproduced with permission [11]. Copyright 2021, Elsevier.

3.3.4. Lasers

The application of TMDs as saturable absorbers (SAs) for Q-switched operation in fibre lasers has been explored and investigated due to their strong photoluminescence, ultrafast carrier dynamics in monolayer and few-layer forms, and semiconducting ability to have a tuneable band gap from the visible to the near-infrared region [79,80]. Alloying TMD materials by adjusting the composition of metallic (MX2) or sulphur (X) elements allows for more precise tuning of the energy band structure of TMDs to better exploit their potential as optoelectronic devices. TMD alloys likewise offer a variety of advantages that are highly favourable for saturable absorption applications, as well as good thermodynamic and environmental stability. Wang et al. in 2018 demonstrated the use of $Mo_{0.5}W_{0.5}S_2$ as an optoelectronic device by using a microwave-assisted solvothermal method to fabricate $Mo_{0.5}W_{0.5}S_2$ and reported for the first time the use of $Mo_{0.5}W_{0.5}S_2$ polymer film and tapered fibre as SA for Q-switched Yb-doped fibre lasers. The modulation depth and saturable intensity of the film SA were 5.63% and 6.82 MW cm^{-2}. A $Mo_{0.5}W_{0.5}S_2$-PVA film SA yielding Q-switched pulses with a pulse energy of 148.8 nJ was realised. The minimum pulse duration was 1.22 µs. A higher pulse energy of 339 nJ and pulse width of 1.46 µs and a higher pulse energy of 339 nJ and pulse width of 1.46 µs were also obtained with the fibre-taper $Mo_{0.5}W_{0.5}S_2$ SA. In addition, they compared $Mo_{0.5}W_{0.5}S_2$ SA with MoS_2 and WS_2 SA, and $Mo_{0.5}W_{0.5}S_2$ SA had a narrower pulse width and was superior in terms of single-pulse energy [13]. Ahmad et al. were able to generate stable Q-switched pulses in the 1.0 µm, 1.5 µm, and 2 µm regions using $MoWSe_2$ alloy as an all-fibre passively Q-switched Yb-, Er-, and Tm-doped fibre laser. $MoWSe_2$ SA performance did not show any degradation over time, demonstrating its potential and applicability as a novel 2D broadband SA material [81]. Yin et al. reported the first realisation of femtosecond photonics of $Mo_{0.5}W_{0.5}S_2$ SA in 2022, suggesting that it is a good candidate for the mode-locked ultrafast fibre laser for optoelectronic and optical communication applications [82]. Niu et al. prepared 2D $MoWS_2$ by using the CVD method and liquid-phase glass method and proposed an LD-pumped doubly Q-switched mode-locked (QML) Tm:YAP laser at a waveband using $MoWS_2$ SA and EOM. In comparison to the single QML laser with

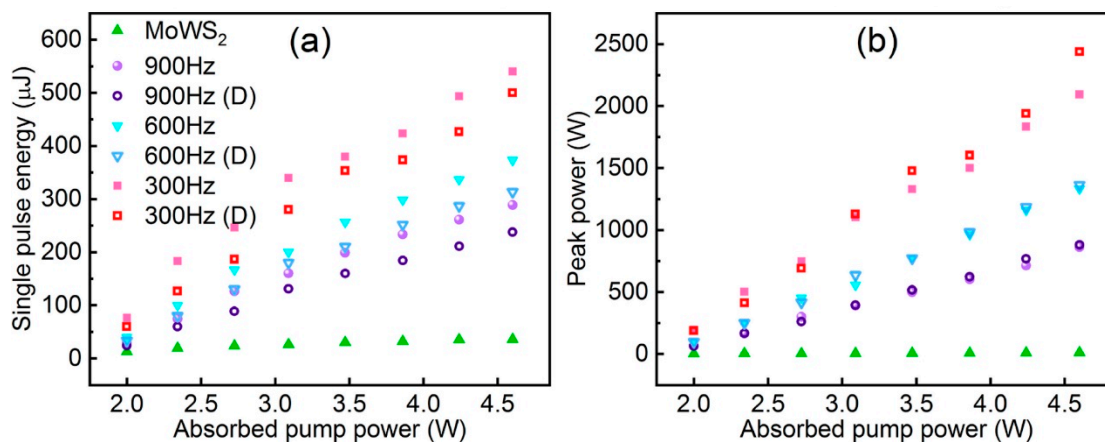MoWS$_2$ SA or EOM, the laser could produce a shorter pulse duration and higher peak power (Figure 18) [83].

Figure 18. (**a**) Single pulse energy and (**b**) pulse peak power of Q-switching envelope versus absorbed pump power. Reproduced with permission [83] Copyright 2022, Elsevier.

3.3.5. Others

Due to their excellent properties, 2D alloyed TMDs have many promising applications in other fields. Ghazanfari et al. prepared for the first time highly sensitive and selective electrochemical sensors based on screen-printed electrodes (MoWS$_2$/SPE) modified with MoWS$_2$ nanoparticles. The MoWS$_2$/SPE showed excellent performance in both electrocatalytic activity and selectivity determination and has been demonstrated to be suitable for the determination of target analytes in tap water and food samples [84]. Ko et al. analysed the effect of the Mo$_x$W$_{1-x}$S$_2$ microstructure on resistance and the temperature coefficient of resistance (TCR) by using I–V measurements. They vulcanised MoW alloys at 800–850 °C to convert the metal layers into Mo$_x$W$_{1-x}$S$_2$ compound semiconductor films. They measured the temperature-dependent I–V characteristics of the samples in the range of 290–570 K and calculated the resistance based on the results. The well-crystallised Mo$_x$W$_{1-x}$S$_2$ thin films after sulphurisation at 950 °C showed a TCR as high as –1.633%/K, which demonstrated their potential for further development and application in thermal sensors [85]. The realisation of superlubrication at metal–metal friction interfaces is a bottleneck that needs to be solved in modern industry. Jiang et al. reduced the coefficient of friction of steel–steel in dry argon to 0.008 by using a graphene and MoWS$_4$ nanosheets heterojunction, which reduces metal-to-metal adhesion and direct contact and provides a new research route for solid lubricant development. In addition to the traditional TMD film structure, there are also 2D molecular layer vertically assembled TMDs [86]. Compared to the film structure, vertically assembled TMDs better expose the layer edge position rather than the basal surface and show anisotropic carrier transport properties. This vertically assembled form provides a feasible idea for the development and application of a TMD alloy. Heterojunctions in which the band gap of one semiconductor lies entirely within the band gap of another semiconductor are type I heterojunctions, which are preferred for luminescence applications. Zhou et al. demonstrated that type I heterojunctions can be realised through the use of interlayer alloying and/or monolayer rotation by means of an ab initio density functional theory approach [87]. He et al. provided high reversible capacities of 517.4 and 362.4 mAh g^{-1} at 100 and 1000 mA g^{-1}, respectively, when optimised vacancy-rich MoSSe alloys were used as anodes for potassium ion batteries. [88]

In accordance with the above applications, TMD alloys are yet to be developed for applications in imaging [89], metamaterials [90], etc., which are areas also in need of development.

4. Conclusions

Two-dimensional TMDs materials have attracted much attention in the fields of microelectronics, catalysis, and optoelectronic devices because of their tuneable band width, carrier migration type, excellent electrical and thermal conductivity, and rich optoelectronic properties. We present a comprehensive review of 2D TMDs alloy materials, including their development and characterisation methods, optoelectronic properties, and applications. In addition to HER and FET, their potential for development in areas such as batteries, lasers, imaging, lubricants, etc., cannot be underestimated. Opportunities and obstacles for future study in the field are focused on the following:

- The research on 2D alloy materials, such as transition metal-sulphur compounds, focuses on the formation of single-layer or few-layer alloy materials, the regulation of band gap and carrier migration types, electrochemical hydrogen precipitation, and optoelectronic devices. Research on bulk phase alloy materials is relatively scarce, and there is an urgent need to find new outlets for applications.
- Insufficient research has been conducted to investigate the preparation of 2D alloy materials with special morphology or morphology control, as well as their corresponding optoelectronic properties.
- The existing approach for regulating alloy concentration involves a singular method that is determined solely by the feeding ratio. In the field of catalysis, it is necessary to explore methods of alloy doping that can increase the number of active sites. Additionally, it is recommended to develop single-atom catalysts.
- Maintaining the enduring stability and dependability of TMDs alloys for diverse applications like electronics and catalysis continues to pose a challenge, particularly in demanding conditions.

TMDs alloy materials have seen compelling progress. They have a wealth of development opportunities in applications such as flexible electronics, quantum technology, heterostructures, and biomedical sensing. However, challenges remain in terms of precise compositional analysis, defect characterisation, scalability, stability, and integration, which must be overcome to realise their full potential in various fields.

Conflicts of Interest: The authors declare no conflict of interest.

References

1. Duan, X.; Wang, C.; Fan, Z.; Hao, G.; Kou, L.; Halim, U.; Li, H.; Wu, X.; Wang, Y.; Jiang, J. Synthesis of $WS_{2x}Se_{2-2x}$ alloy nanosheets with composition-tunable electronic properties. *Nano Lett.* **2016**, *16*, 264–269. [CrossRef] [PubMed]
2. Cui, F.; Feng, Q.; Hong, J.; Wang, R.; Bai, Y.; Li, X.; Liu, D.; Zhou, Y.; Liang, X.; He, X. Synthesis of Large-Size 1T′ $ReS_{2x}Se_{2(1-x)}$ Alloy Monolayer with Tunable Bandgap and Carrier Type. *Adv. Mater.* **2017**, *29*, 1705015. [CrossRef]
3. Xi, J.; Zhao, T.; Wang, D.; Shuai, Z. Tunable electronic properties of two-dimensional transition metal dichalcogenide alloys: A first-principles prediction. *J. Phys. Chem. Lett.* **2014**, *5*, 285–291. [CrossRef] [PubMed]
4. Wen, W.; Zhu, Y.; Liu, X.; Hsu, H.P.; Fei, Z.; Chen, Y.; Wang, X.; Zhang, M.; Lin, K.H.; Huang, F.S. Anisotropic spectroscopy and electrical properties of 2D $ReS_{2(1-x)}Se_{2x}$ alloys with distorted 1T structure. *Small* **2017**, *13*, 1603788. [CrossRef]
5. Lavrov, S.; Shestakova, A.; Avdizhiyan, A.; Abdullaev, D.; Mishina, E.; Sushkevich, K.; Kulyuk, L. The heterogeneity analysis of two-dimensional $Mo_{(1-x)}W_{(x)}S_{(1-y)}$ Sey alloys by optical methods. *Thin Solid. Film.* **2018**, *651*, 7–12. [CrossRef]
6. Kwon, I.S.; Kwak, I.H.; Debela, T.T.; Kim, J.Y.; Yoo, S.J.; Kim, J.-G.; Park, J.; Kang, H.S. Phase-Transition $Mo_{1-x}V_xSe_2$ Alloy Nanosheets with Rich V–Se Vacancies and Their Enhanced Catalytic Performance of Hydrogen Evolution Reaction. *ACS Nano* **2021**, *15*, 14672–14682. [CrossRef]
7. Kwak, I.H.; Kwon, I.S.; Kim, J.Y.; Zewdie, G.M.; Lee, S.J.; Yoo, S.J.; Kim, J.-G.; Park, J.; Kang, H.S. Full Composition Tuning of $W_{1-x}Nb_xSe_2$ Alloy Nanosheets to Promote the Electrocatalytic Hydrogen Evolution Reaction. *ACS Nano* **2022**, *16*, 13949–13958. [CrossRef] [PubMed]
8. Zhang, Y.; Liu, K.; Wang, F.; Shifa, T.A.; Wen, Y.; Wang, F.; Xu, K.; Wang, Z.; Jiang, C.; He, J. Dendritic growth of monolayer ternary $WS_{2(1-x)}Se_{2x}$ flakes for enhanced hydrogen evolution reaction. *Nanoscale* **2017**, *9*, 5641–5647. [CrossRef]

9. Sun, H.; Zhou, X.; Wang, X.; Xu, L.; Zhang, J.; Jiang, K.; Shang, L.; Hu, Z.; Chu, J. P–N conversion of charge carrier types and high photoresponsive performance of composition modulated ternary alloy W (S$_x$Se$_{1−x}$)$_2$ field-effect transistors. *Nanoscale* **2020**, *12*, 15304–15317. [CrossRef]

10. Sanjay, S.; Ganapathi, K.L.; Varrla, E.; Bhat, N. Performance tunability of field-effect transistors using MoS$_{2(1−x)}$Se$_{2x}$ alloys. *Nanotechnology* **2021**, *32*, 435202. [CrossRef]

11. Bhoyate, S.; Park, B.; Oh, S.H.; Choi, W. Defect engineered MoWS alloy catalyst boost the polysulfide conversion in lithium–sulfur battery. *J. Power Sources* **2021**, *511*, 230426. [CrossRef]

12. Feng, W.; Zhao, Z.; Lei, Z.; Zhang, L. MoWS$_2$ Nanosheet Composite with MXene as Lithium-Sulfur Battery Cathode Material. *Adv. Mater. Sci. Eng.* **2023**, *2023*, 6211780. [CrossRef]

13. Wang, J.; Chen, L.; Dou, C.; Yan, H.; Meng, L.; Wei, Z. Mo0. 5W0. 5S2 for Q-switched pulse generation in ytterbium-doped fiber laser. *Nanotechnology* **2018**, *29*, 224002. [CrossRef] [PubMed]

14. Averchenko, A.V.; Salimon, I.A.; Zharkova, E.V.; Lipovskikh, S.; Somov, P.; Abbas, O.A.; Lagoudakis, P.G.; Mailis, S. Laser-enabled localized synthesis of Mo$_{1−x}$WxS$_2$ alloys with tunable composition. *Mater. Today Adv.* **2023**, *17*, 100351. [CrossRef]

15. Kiran, V.; Mukherjee, D.; Jenjeti, R.N.; Sampath, S. Active guests in the MoS$_2$/MoSe$_2$ host lattice: Efficient hydrogen evolution using few-layer alloys of MoS$_{2(1−x)}$Se$_{2x}$. *Nanoscale* **2014**, *6*, 12856–12863. [CrossRef] [PubMed]

16. Chen, Y.; Xi, J.; Dumcenco, D.O.; Liu, Z.; Suenaga, K.; Wang, D.; Shuai, Z.; Huang, Y.S.; Xie, L. Tunable band gap photolumines-cence from atomically thin transition-metal dichalcogenide alloys. *ACS Nano* **2013**, *7*, 4610–4616. [CrossRef] [PubMed]

17. Zhang, M.; Wu, J.X.; Zhu, Y.M.; Dumcenco, D.O.; Hong, J.H.; Mao, N.N.; Deng, S.B.; Chen, Y.F.; Yang, Y.L.; Jin, C.H.; et al. Two-Dimensional Molybdenum Tungsten Diselenide Alloys: Photoluminescence, Raman Scattering, and Electrical Transport. *Acs Nano* **2014**, *8*, 7130–7137. [CrossRef]

18. Wang, Z.; Liu, P.; Ito, Y.; Ning, S.; Tan, Y.; Fujita, T.; Hirata, A.; Chen, M. Chemical Vapor Deposition of Monolayer Mo$_{(1−x)}$W$_{(x)}$S$_2$ Crystals with Tunable Band Gaps. *Sci. Rep.* **2016**, *6*, 21536. [CrossRef]

19. Zhou, J.; Lin, J.; Huang, X.; Zhou, Y.; Chen, Y.; Xia, J.; Wang, H.; Xie, Y.; Yu, H.; Lei, J.; et al. A library of atomically thin metal chalcogenides. *Nature* **2018**, *556*, 355–359. [CrossRef]

20. Feng, Q.L.; Mao, N.N.; Wu, J.X.; Xu, H.; Wang, C.M.; Zhang, J.; Xie, L.M. Growth of MoS$_{2(1−x)}$Se$_{2x}$ (x = 0.41–1.00) Monolayer Alloys with Controlled Morphology by Physical Vapor Deposition. *Acs Nano* **2015**, *9*, 7450–7455. [CrossRef]

21. Feng, Q.; Zhu, Y.; Hong, J.; Zhang, M.; Duan, W.; Mao, N.; Wu, J.; Xu, H.; Dong, F.; Lin, F.; et al. Growth of large-area 2D MoS$_{2(1−x)}$Se$_{2x}$ semiconductor alloys. *Adv. Mater.* **2014**, *26*, 2648–2653+2613. [CrossRef]

22. Zhang, L.; Yang, T.; He, X.; Zhang, W.; Vinai, G.; Tang, C.S.; Yin, X.; Torelli, P.; Feng, Y.P.; Wong, P.K.J.; et al. Molecular Beam Epitaxy of Two-Dimensional Vanadium-Molybdenum Diselenide Alloys. *ACS Nano* **2020**, *14*, 11140–11149. [CrossRef] [PubMed]

23. Song, J.G.; Ryu, G.H.; Lee, S.J.; Sim, S.; Lee, C.W.; Choi, T.; Jung, H.; Kim, Y.; Lee, Z.; Myoung, J.M.; et al. Controllable synthesis of molybdenum tungsten disulfide alloy for vertically composition-controlled multilayer. *Nat. Commun.* **2015**, *6*, 7817. [CrossRef]

24. Yu, Y.; Hu, S.; Su, L.; Huang, L.; Liu, Y.; Jin, Z.; Purezky, A.A.; Geohegan, D.B.; Kim, K.W.; Zhang, Y.; et al. Equally efficient interlayer exciton relaxation and improved absorption in epitaxial and nonepitaxial MoS$_2$/WS$_2$ heterostructures. *Nano Lett.* **2015**, *15*, 486–491. [CrossRef] [PubMed]

25. Tongay, S.; Fan, W.; Kang, J.; Park, J.; Koldemir, U.; Suh, J.; Narang, D.S.; Liu, K.; Ji, J.; Li, J.; et al. Tuning interlayer coupling in large-area heterostructures with CVD-grown MoS$_2$ and WS$_2$ monolayers. *Nano Lett.* **2014**, *14*, 3185–3190. [CrossRef]

26. Gong, Y.; Lin, J.; Wang, X.; Shi, G.; Lei, S.; Lin, Z.; Zou, X.; Ye, G.; Vajtai, R.; Yakobson, B.I.; et al. Vertical and in-plane heterostructures from WS$_2$/MoS$_2$ monolayers. *Nat. Mater.* **2014**, *13*, 1135–1142. [CrossRef] [PubMed]

27. Chiu, M.H.; Li, M.Y.; Zhang, W.J.; Hsu, W.T.; Chang, W.H.; Terrones, M.; Terrones, H.; Li, L.J. Spectroscopic Signatures for Interlayer Coupling in MoS$_2$–WSe$_2$ van der Waals Stacking. *Acs Nano* **2014**, *8*, 9649–9656. [CrossRef]

28. Wang, D.; Luo, F.; Lu, M.; Xie, X.; Huang, L.; Huang, W. Chemical Vapor Transport Reactions for Synthesizing Layered Materials and Their 2D Counterparts. *Small* **2019**, *15*, e1804404. [CrossRef]

29. Qian, X.; Jiang, P.; Yu, P.; Gu, X.; Liu, Z.; Yang, R. Anisotropic thermal transport in van der Waals layered alloys WSe$_{2(1−x)}$Te$_{2x}$. *Appl. Phys. Lett.* **2018**, *112*, 241901. [CrossRef]

30. Su, W.-J.; Weng, W.-Q.; Wang, Y.-L.; Gan, W.-S.; Honda, S.-I.; Chen, R.-S.; Huang, Y.-S.; Lee, K.-Y. Mo$_{1−x}$W$_x$S$_2$-based photodetector fabrication and photoconductive characteristics. *Jpn. J. Appl. Phys.* **2017**, *56*, 32201. [CrossRef]

31. Schmidt, P.; Binnewies, M.; Glaum, R.; Schmidt, M. *Chemical Vapor Transport Reactions–Methods, Materials, Modeling*; InTech: Rijeka, Croatia, 2013.

32. Tan, C.; Cao, X.; Wu, X.J.; He, Q.; Yang, J.; Zhang, X.; Chen, J.; Zhao, W.; Han, S.; Nam, G.H.; et al. Recent Advances in Ultrathin Two-Dimensional Nanomaterials. *Chem. Rev.* **2017**, *117*, 6225–6331. [CrossRef]

33. Vaidya, R.; Dave, M.; Patel, S.S.; Patel, S.G.; Jani, A.R. Growth of molybdenum disulphide using iodine as transport material. *Pramana* **2004**, *63*, 611–616. [CrossRef]

34. Wang, Y.; Huang, L.; Li, B.; Shang, J.; Xia, C.; Fan, C.; Deng, H.-X.; Wei, Z.; Li, J. Composition-tunable 2D SnSe$_{2(1−x)}$S$_{2x}$ alloys towards efficient bandgap engineering and high performance (opto) electronics. *J. Mater. Chem. C* **2017**, *5*, 84–90. [CrossRef]

35. Fali, A.; Zhang, T.; Terry, J.P.; Kahn, E.; Fujisawa, K.; Kabius, B.; Koirala, S.; Ghafouri, Y.; Zhou, D.; Song, W.; et al. Photodegrada-tion protection in 2D in-plane heterostructures revealed by hyperspectral nanoimaging: The role of nanointerface 2D alloys. *ACS Nano* **2021**, *15*, 2447–2457. [CrossRef] [PubMed]

36. Chen, Y.; Dumcenco, D.O.; Zhu, Y.; Zhang, X.; Mao, N.; Feng, Q.; Zhang, M.; Zhang, J.; Tan, P.H.; Huang, Y.S.; et al. Composition-dependent Raman modes of $Mo_{(1-x)}W_{(x)}S_2$ monolayer alloys. *Nanoscale* **2014**, *6*, 2833–2839. [CrossRef]

37. Fan, X.; Zhao, Y.; Zheng, W.; Li, H.; Wu, X.; Hu, X.; Zhang, X.; Zhu, X.; Zhang, Q.; Wang, X.; et al. Controllable Growth and Formation Mechanisms of Dislocated WS_2 Spirals. *Nano Lett.* **2018**, *18*, 3885–3892. [CrossRef] [PubMed]

38. Zhang, J.; Wang, J.; Chen, P.; Sun, Y.; Wu, S.; Jia, Z.; Lu, X.; Yu, H.; Chen, W.; Zhu, J.; et al. Observation of Strong Interlayer Coupling in MoS_2/WS_2 Heterostructures. *Adv. Mater.* **2016**, *28*, 1950–1956. [CrossRef]

39. Koma, A. Van der Waals epitaxy for highly lattice-mismatched systems. *J. Cryst. Growth* **1999**, *201*, 236–241. [CrossRef]

40. Melitz, W.; Shen, J.; Kummel, A.C.; Lee, S. Kelvin probe force microscopy and its application. *Surf. Sci. Rep.* **2011**, *66*, 1–27. [CrossRef]

41. Hu, Z.; Yin, Z.; Yin, Z.; Wang, K.; Liu, Q.; Sun, P.; Yan, H.; Song, H.; Luo, C.; Guan, H. Corrosion behavior characterization of as extruded Mg-8Li-3Al alloy with minor alloying elements (Gd, Sn and Cu) by scanning Kelvin probe force microscopy. *Corros. Sci.* **2020**, *176*, 108923. [CrossRef]

42. Örnek, C.; Leygraf, C.; Pan, J. Passive film characterisation of duplex stainless steel using scanning Kelvin probe force microscopy in combination with electrochemical measurements. *Npj Mater. Degrad.* **2019**, *3*, 8. [CrossRef]

43. Rosenwaks, Y.; Shikler, R.; Glatzel, T.; Sadewasser, S. Kelvin probe force microscopy of semiconductor surface defects. *Phys. Rev. B* **2004**, *70*, 085320. [CrossRef]

44. Adachi, Y.; Wen, H.F.; Zhang, Q.; Miyazaki, M.; Sugawara, Y.; Li, Y.J. Elucidating the charge state of an Au nanocluster on the oxidized/reduced rutile TiO_2 (110) surface using non-contact atomic force microscopy and Kelvin probe force microscopy. *Nanoscale Adv.* **2020**, *2*, 2371–2375. [CrossRef] [PubMed]

45. Liu, P.; Li, H.; Yang, L.; Zhao, B.; Li, M.; Xiang, B. Rational synthesis of bandgap-tunable $MS_{2(1-x)}Se_{2x}$ (M = Mo, W) alloys and their physical properties. *J. Alloys Compd.* **2017**, *710*, 628–634. [CrossRef]

46. Samaniego-Benitez, J.E.; Mendoza-Cruz, R.; Bazán-Díaz, L.; Garcia-Garcia, A.; Arellano-Jimenez, M.J.; Perez-Robles, J.F.; Plascencia-Villa, G.; Velázquez-Salazar, J.J.; Ortega, E.; Favela-Camacho, S.E.; et al. Synthesis and structural characterization of MoS_2 micropyramids. *J. Mater. Sci.* **2020**, *55*, 12203–12213. [CrossRef]

47. Puretzky, A.A.; Liang, L.B.; Li, X.F.; Xiao, K.; Wang, K.; Mahjouri-Samani, M.; Basile, L.; Idrobo, J.C.; Sumpter, B.G.; Meunier, V.; et al. Low-Frequency Raman Fingerprints of Two-Dimensional Metal Dichalcogenide Layer Stacking Configurations. *Acs Nano* **2015**, *9*, 6333–6342. [CrossRef]

48. Qiao, X.-F.; Li, X.-L.; Zhang, X.; Shi, W.; Wu, J.-B.; Chen, T.; Tan, P.-H. Substrate-free layer-number identification of two-dimensional materials: A case of $Mo_{0.5}W_{0.5}S_2$ alloy. *Appl. Phys. Lett.* **2015**, *106*, 223102. [CrossRef]

49. Zhang, X.; Qiao, X.F.; Shi, W.; Wu, J.B.; Jiang, D.S.; Tan, P.H. Phonon and Raman scattering of two-dimensional transition metal dichalcogenides from monolayer, multilayer to bulk material. *Chem. Soc. Rev.* **2015**, *44*, 2757–2785. [CrossRef]

50. Chen, Y.; Wen, W.; Zhu, Y.; Mao, N.; Feng, Q.; Zhang, M.; Hsu, H.P.; Zhang, J.; Huang, Y.S.; Xie, L. Temperature-dependent photoluminescence emission and Raman scattering from $Mo_{1-x}W_xS_2$ monolayers. *Nanotechnology* **2016**, *27*, 445705. [CrossRef]

51. Xie, L.M. Two-dimensional transition metal dichalcogenide alloys: Preparation, characterization and applications. *Nanoscale* **2015**, *7*, 18392–18401. [CrossRef]

52. Eda, G.; Yamaguchi, H.; Voiry, D.; Fujita, T.; Chen, M.; Chhowalla, M. Photoluminescence from chemically exfoliated MoS_2. *Nano Lett.* **2011**, *11*, 5111–5116. [CrossRef]

53. Late, D.J.; Liu, B.; Matte, H.; Dravid, V.P.; Rao, C.N.R. Hysteresis in Single-Layer MoS_2 Field Effect Transistors. *Acs Nano* **2012**, *6*, 5635–5641. [CrossRef]

54. Warner, J.H.; Rummeli, M.H.; Bachmatiuk, A.; Buchner, B. Atomic Resolution Imaging and Topography of Boron Nitride Sheets Produced by Chemical Exfoliation. *ACS Nano* **2010**, *4*, 1299–1304. [CrossRef]

55. Alfalasi, W.; Al Qasir, I.; Tit, N. Origins of bandgap bowing character in the common-anion transition-metal-dichalcogenide ternary alloyed monolayer: Ab initio investigation. *New J. Phys.* **2021**, *23*, 103027. [CrossRef]

56. Dumcenco, D.O.; Su, Y.C.; Wang, Y.P.; Chen, K.Y.; Huang, Y.S.; Ho, C.H.; Tiong, K.K. Polarization Dependent Raman Active Modes Study of the $Mo_{1-x}W_xS_2$ Mixed Layered Crystals. *Chin. J. Phys.* **2011**, *49*, 270–277.

57. Dumcenco, D.O.; Kobayashi, H.; Liu, Z.; Huang, Y.S.; Suenaga, K. Visualization and quantification of transition metal atomic mixing in $Mo_{1-x}WxS_2$ single layers. *Nat. Commun.* **2013**, *4*, 1351. [CrossRef]

58. Komsa, H.P.; Krasheninnikov, A.V. Two-Dimensional Transition Metal Dichalcogenide Alloys: Stability and Electronic Properties. *J. Phys. Chem. Lett.* **2012**, *3*, 3652–3656. [CrossRef]

59. Voiry, D.; Mohite, A.; Chhowalla, M. Phase engineering of transition metal dichalcogenides. *Chem. Soc. Rev.* **2015**, *44*, 2702–2712. [CrossRef]

60. Wang, Z.; Sun, J.; Wang, H.; Lei, Y.; Xie, Y.; Wang, G.; Zhao, Y.; Li, X.; Xu, H.; Yang, X. 2H/1T′ phase $WS_{2(1-x)}Te_{2x}$ alloys grown by chemical vapor deposition with tunable band structures. *Appl. Surf. Sci.* **2020**, *504*, 144371. [CrossRef]

61. Tan, C.; Zhao, W.; Chaturvedi, A.; Fei, Z.; Zeng, Z.; Chen, J.; Huang, Y.; Ercius, P.; Luo, Z.; Qi, X. Preparation of single-layer $MoS_{2x}Se_{2(1-x)}$ and $Mo_xW_{1-x}S_2$ nanosheets with high-concentration metallic 1T phase. *Small* **2016**, *12*, 1866–1874. [CrossRef]

62. Apte, A.; Kochat, V.; Rajak, P.; Krishnamoorthy, A.; Manimunda, P.; Hachtel, J.A.; Idrobo, J.C.; Syed Amanulla, S.A.; Vashishta, P.; Nakano, A. Structural phase transformation in strained monolayer $MoWSe_2$ alloy. *ACS Nano* **2018**, *12*, 3468–3476. [CrossRef] [PubMed]

63. Zhang, F.; Zhang, H.; Krylyuk, S.; Milligan, C.A.; Zhu, Y.; Zemlyanov, D.Y.; Bendersky, L.A.; Burton, B.P.; Davydov, A.V.; Appenzeller, J. Electric-field induced structural transition in vertical MoTe$_2$-and Mo$_{1-x}$W$_x$Te$_2$-based resistive memories. *Nat. Mater.* **2019**, *18*, 55–61. [CrossRef] [PubMed]

64. Tayebi, M.; Masoumi, Z.; Kolaei, M.; Tayyebi, A.; Tayebi, M.; Seo, B.; Lim, C.-S.; Kim, H.-G.; Lee, B.-K. Highly efficient and stable WO$_3$/MoS$_2$-MoO$_X$ photoanode for photoelectrochemical hydrogen production; a collaborative approach of facet engineering and PN junction. *Chem. Eng. J.* **2022**, *446*, 136830. [CrossRef]

65. Masoumi, Z.; Tayebi, M.; Kolaei, M.; Lee, B.-K. Efficient and stable core-shell α–Fe$_2$O$_3$/WS$_2$/WO$_x$ photoanode for oxygen evolution reaction to enhance photoelectrochemical water splitting. *Appl. Catal. B Environ.* **2022**, *313*, 121447. [CrossRef]

66. Masoumi, Z.; Tayebi, M.; Kolaei, M.; Lee, B.-K. Unified surface modification by double heterojunction of MoS$_2$ nanosheets and BiVO$_4$ nanoparticles to enhance the photoelectrochemical water splitting of hematite photoanode. *J. Alloys Compd.* **2022**, *890*, 161802. [CrossRef]

67. Masoumi, Z.; Tayebi, M.; Kolaei, M.; Tayyebi, A.; Ryu, H.; Jang, J.I.; Lee, B.-K. Simultaneous enhancement of charge separation and hole transportation in a W: α-Fe$_2$O$_3$/MoS$_2$ photoanode: A collaborative approach of MoS$_2$ as a heterojunction and W as a metal dopant. *ACS Appl. Mater. Interfaces* **2021**, *13*, 39215–39229. [CrossRef] [PubMed]

68. Masoumi, Z.; Tayebi, M.; Lee, B.-K. Ultrasonication-assisted liquid-phase exfoliation enhances photoelectrochemical performance in α-Fe$_2$O$_3$/MoS$_2$ photoanode. *Ultrason. Sonochem.* **2021**, *72*, 105403. [CrossRef]

69. Zhu, J.; Wang, Z.-C.; Dai, H.; Wang, Q.; Yang, R.; Yu, H.; Liao, M.; Zhang, J.; Chen, W.; Wei, Z. Boundary activated hydrogen evolution reaction on monolayer MoS$_2$. *Nat. Commun.* **2019**, *10*, 1348. [CrossRef]

70. Li, J.; Hong, M.; Sun, L.; Zhang, W.; Shu, H.; Chang, H. Enhanced electrocatalytic hydrogen evolution from large-scale, facile-prepared, highly crystalline WTe$_2$ nanoribbons with weyl semimetallic phase. *ACS Appl. Mater. Interfaces* **2018**, *10*, 458–467. [CrossRef]

71. Hu, P.; Long, G.; Chaturvedi, A.; Wang, S.; Tan, K.; He, Y.; Zheng, L.; Liu, G.; Ke, Y.; Zhou, Y. Agent-assisted VSSe ternary alloy single crystals as an efficient stable electrocatalyst for the hydrogen evolution reaction. *J. Mater. Chem. A* **2019**, *7*, 15714–15721. [CrossRef]

72. Kwak, I.H.; Kwon, I.S.; Debela, T.T.; Abbas, H.G.; Park, Y.C.; Seo, J.; Ahn, J.-P.; Lee, J.H.; Park, J.; Kang, H.S. Phase Evolution of Re$_{1-x}$Mo$_x$Se$_2$ Alloy Nanosheets and Their Enhanced Catalytic Activity toward Hydrogen Evolution Reaction. *ACS Nano* **2020**, *14*, 11995–12005. [CrossRef]

73. Kwon, I.S.; Lee, S.J.; Kim, J.Y.; Kwak, I.H.; Zewdie, G.M.; Yoo, S.J.; Kim, J.-G.; Lee, K.-S.; Park, J.; Kang, H.S. Composition-Tuned (MoWV)Se$_2$ Ternary Alloy Nanosheets as Excellent Hydrogen Evolution Reaction Electrocatalysts. *ACS Nano* **2023**, *17*, 2968–2979. [CrossRef]

74. Jin, Y.; Zeng, Z.; Xu, Z.; Lin, Y.-C.; Bi, K.; Shao, G.; Hu, T.S.; Wang, S.; Li, S.; Suenaga, K.; et al. Synthesis and Transport Properties of Degenerate P-Type Nb-Doped WS2 Monolayers. *Chem. Mater.* **2019**, *31*, 3534–3541. [CrossRef]

75. Fang, H.; Tosun, M.; Seol, G.; Chang, T.C.; Takei, K.; Guo, J.; Javey, A. Degenerate n-doping of few-layer transition metal dichalcogenides by potassium. *Nano Lett.* **2013**, *13*, 1991–1995. [CrossRef] [PubMed]

76. Suh, J.; Park, T.E.; Lin, D.Y.; Fu, D.; Park, J.; Jung, H.J.; Chen, Y.; Ko, C.; Jang, C.; Sun, Y.; et al. Doping against the native propensity of MoS$_2$: Degenerate hole doping by cation substitution. *Nano Lett.* **2014**, *14*, 6976–6982. [CrossRef]

77. Zhou, L.; Danilov, D.L.; Qiao, F.; Wang, J.; Li, H.; Eichel, R.A.; Notten, P.H. Sulfur reduction reaction in lithium–sulfur batteries: Mechanisms, catalysts, and characterization. *Adv. Energy Mater.* **2022**, *12*, 2202094. [CrossRef]

78. Liu, D.; Zhang, C.; Zhou, G.; Lv, W.; Ling, G.; Zhi, L.; Yang, Q.H. Catalytic effects in lithium–sulfur batteries: Promoted sulfur transformation and reduced shuttle effect. *Adv. Sci.* **2018**, *5*, 1700270. [CrossRef] [PubMed]

79. Zhang, M.; Hu, G.; Hu, G.; Howe, R.; Chen, L.; Zheng, Z.; Hasan, T. Yb-and Er-doped fiber laser Q-switched with an optically uniform, broadband WS$_2$ saturable absorber. *Sci. Rep.* **2015**, *5*, 17482. [CrossRef]

80. Chen, B.; Zhang, X.; Wu, K.; Wang, H.; Wang, J.; Chen, J. Q-switched fiber laser based on transition metal dichalcogenides MoS 2, MoSe$_2$, WS$_2$, and WSe$_2$. *Opt. Express* **2015**, *23*, 26723–26737. [CrossRef]

81. Ahmad, H.; Reduan, S.A.; Aidit, S.N.; Yusoff, N.; Maah, M.J.; Ismail, M.F.; Tiu, Z.C. Ternary MoWSe$_2$ alloy saturable absorber for passively Q-switched Yb-, Er-and Tm-doped fiber laser. *Opt. Commun.* **2019**, *437*, 355–362. [CrossRef]

82. Lei, J.; Wang, J.; Wang, X.; Wei, Z. Ternary 2D Mo$_{(1-x)}$WxS$_2$ as a saturable absorber for femtosecond mode-locked all fiber lasers. *Opt. Laser Technol.* **2022**, *145*, 107482. [CrossRef]

83. Niu, Z.; Feng, T.; Li, T.; Yang, K.; Zhao, J.; Li, G.; Li, D.; Zhao, S.; Qiao, W.; Chu, H. Doubly Q-switched mode-locked Tm: YAP laser at 2μm with ternary MoWS2 alloy and EOM. *Opt. Commun.* **2022**, *520*, 128544. [CrossRef]

84. Ghazanfari, Z.; Sarhadi, H.; Tajik, S. Determination of Sudan I and bisphenol A in tap water and food samples using electrochemical nanosensor. *Surf. Eng. Appl. Electrochem.* **2021**, *57*, 397–407. [CrossRef]

85. Ko, T.-S.; Lin, E.-T.; Huang, X.-W.; Wu, P.-T.; Yang, Y.-L. High-Temperature Coefficient of Resistance in Mo$_x$W$_{1-x}$S$_2$ Thin Film. *Appl. Sci.* **2022**, *12*, 5110. [CrossRef]

86. Jung, Y.; Shen, J.; Sun, Y.; Cha, J.J. Chemically synthesized heterostructures of two-dimensional molybdenum/tungsten-based dichalcogenides with vertically aligned layers. *ACS Nano* **2014**, *8*, 9550–9557. [CrossRef] [PubMed]

87. Zhou, S.; Ning, J.; Sun, J.; Srolovitz, D.J. Composition-induced type I and direct bandgap transition metal dichalcogenides alloy vertical heterojunctions. *Nanoscale* **2020**, *12*, 201–209. [CrossRef]

88. He, H.; Huang, D.; Gan, Q.; Hao, J.; Liu, S.; Wu, Z.; Pang, W.K.; Johannessen, B.; Tang, Y.; Luo, J.-L. Anion vacancies regulating endows MoSSe with fast and stable potassium ion storage. *ACS Nano* **2019**, *13*, 11843–11852. [CrossRef]

89. Sepehripour, F.; Alavijeh, A.S.; Fakharzadeh, M.; Khavasi, A. A broadband and compact millimeter-wave imaging system based on synthetic aperture radar. *arXiv* **2022**, arXiv:2205.14707.

90. Sepehripour, F.; Karimi, P.; Khavasi, A. Wideband and polarisation-independent antireflection coating using metamaterials. *IET Optoelectron.* **2020**, *14*, 266–273. [CrossRef]